

INTEGRAL Observations of the 2010 Cygnus X-1 Soft State

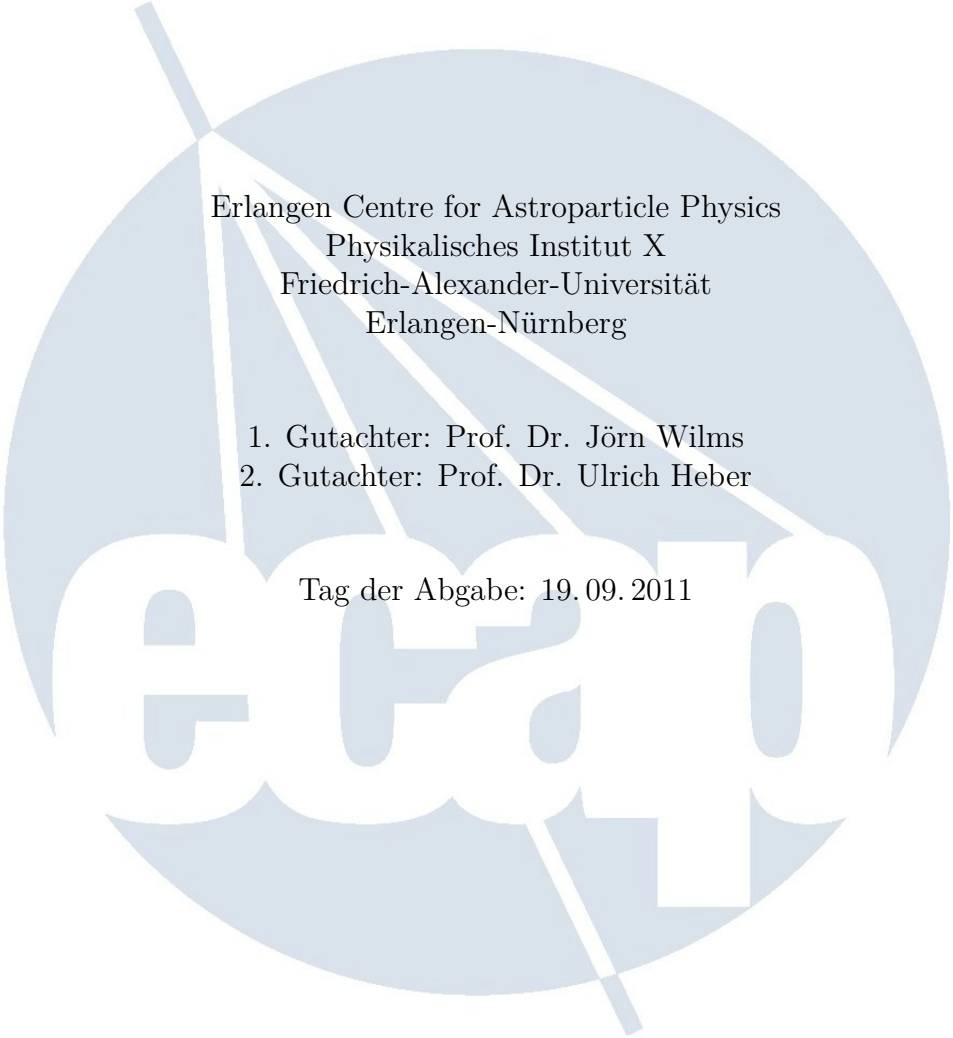
Bachelorarbeit

vorgelegt von
Alexander Popp

Erlangen Centre for Astroparticle Physics
Physikalisches Institut X
Friedrich-Alexander-Universität
Erlangen-Nürnberg

1. Gutachter: Prof. Dr. Jörn Wilms
2. Gutachter: Prof. Dr. Ulrich Heber

Tag der Abgabe: 19.09.2011



eacap

Contents

1	Introduction	2
1.1	First Detection of Cygnus X-1	2
1.2	Cygnus X-1 and the big picture	2
1.2.1	The Importance	2
1.2.2	Accretions Process	3
1.2.3	The Jet	3
1.2.4	Hard and Soft State - the q-Track	4
2	Methodes of Observation	7
2.1	High Energy Observations	7
2.2	INTEGRAL Satellite	7
3	Data Reduction	11
3.1	IBIS	11
3.1.1	Images and Mosaics	11
3.1.2	Spectra	12
3.2	JEMX	13
4	Summary of all available Data	14
4.1	Data Overview	14
4.2	A Closer Look	14
5	Spectral Analysis	17
5.1	Spectral Analysis Basics	17
5.2	Fit Functions	17
5.3	ISGRI	18
5.3.1	First Results	19
5.3.2	Search for the Hard Tail - Strange Residuals	20
5.3.3	Assessing the Calibration Problems	21
5.4	JEM-X	25
5.5	Combined Spectra of ISGRI and JEMX	27
6	Summary and Discussion	31
6.1	ISGRI	31
6.2	Overall Data	31
A	Appendix	33

Abstract

The galactic X-ray source Cygnus X-1 is a black hole in a binary system with the companion star HD 226868. Its behavior as an accreting black hole is similar to the behavior of AGN and due to the different mass scales the longtime evolution of such accreting objects can be studied by observing Cygnus X-1. Accreting black holes show different accretion states, which can be described in the so-called q-track in a hardness-intensity diagram. One of the states is the soft state, where the hard X-ray spectrum has a power law slope with $\Gamma > 2$ and the radio activity is suppressed, and the last soft state (from August'10 to March'11) is the topic of this thesis. The high energy X-rays from Cygnus X-1 were detected by two coded mask instruments on board the *INTEGRAL* satellite. The first data for this work come from the ISGRI detector, a part of the IBIS instrument and the additional data come from the two JEM-X instruments of *INTEGRAL*.

The extracted count rates were compared with data from other astronomical devices, especially radio data from the AMI telescope to assess the behavior of the source at different energies.

The spectra of the reduced data of the ISGRI detector were modelled with different empirical and physically motivated models. All fits are dominated by characteristic residuals which are due to calibration problems. Two flavors of the soft state were found in the best fit parameters of all three models, the flavor with the higher hardness seems to be coincident with a higher radio activity at the same time. Also hard tails were not found in the summed spectra due to the bad residuals.

Tests with a non-released test version of the next version of the ARF (courtesy of the *INTEGRAL* calibration team) were done, which generated mostly better fit results but also some not yet understood effects. The extraction of only the data in the fully coded field of view did not improve the fit results.

The data of the two JEM-X instruments were reduced and modelled. The spectra of the ISGRI and the JEM-X instruments were matched together and modeled with a broken power law and a simple Comptonization model, which both can describe the combined spectra well.

The results were compared to the data from Wilms et al. (2006), who analyzed RXTE spectra of Cygnus X-1. The parameter ranges are mostly consistent within the error bars, but show deviations. In conclusion the *INTEGRAL* data can be compared with data from other devices, but due to the bad residuals the work has to be repeated when a new version of the OSA software with a better working ARF is released, especially to search for possible high energy excesses.

Chapter 1

Introduction

In this chapter the historic discovery of Cygnus X-1 will be outlined. And furthermore the object Cygnus X-1, its characteristics and its importance for the science will be pointed out in a short description to establish the basics needed for this thesis.

1.1 First Detection of Cygnus X-1

In the year 1964 eight bright new cosmic X-ray sources were detected by the two Aerobee surveys, which sounded out the sky for X-ray sources (Bowyer et al., 1965). This was the first detection of the Cygnus X-1. After that Uhuru, the first X-ray satellite orbiting the Earth (from 1970 to 1973), observed inter alia Cygnus X-1 (<http://heasarc.gsfc.nasa.gov/docs/uhuru/uhuru.html>).

First, it was only known that the star HDE 226868 was the source of the bright X-ray and also of the detected radio flares. Measurements of its radial velocity, done by Webster & Murdin (1972), have shown a variability of the velocity correlating with the known changes of the X-ray flux. This shows the binary behavior of this system with a period of 5.6 days (Webster & Murdin, 1972). The the star HD 226868 estimated to be an star with many solar masses and so the compact component needed also a high mass to explain the variable radial velocity. Herrero et al. (1995) used unified models to calculate the Mass of the star HDE 226868 to $17.8 M_{\odot}$ and of the compact companion to $10 M_{\odot}$. There were many other measurements, for example HDE 226868 $40 \pm 5 M_{\odot}$ and Cygnus X-1 $20 \pm 5 M_{\odot}$ (Ziółkowski, 2005) or HDE 226868 $14-19 M_{\odot}$ and Cygnus X-1 $5-12 M_{\odot}$ (Hutchings, 1978), of the mass of the binary system components but all say that the compact object has a mass bigger than a neutron star could have (Oppenheimer & Volkoff, 1939, maximum Oppenheimer-Volkoff limit of around $3 M_{\odot}$).

1.2 Cygnus X-1 and the big picture

1.2.1 The Importance

Why Cygnus X-1? Now some facts of the discovery of Cygnus X-1 are known and also that it only can be a black hole and the star HD 226868 is its companion in a binary star system. To answer the question above, what Cygnus X-1 stands for is needed to know.

Black holes can not be observed directly because even light can not escape from them. But the radiation emitted from gas falling into the black hole is observable. In binary systems, gas from the companion star can stream to the black hole and forms an accretions disc. The inner part of this disc finally falls into the black hole. The radiation observed by the detectors has its

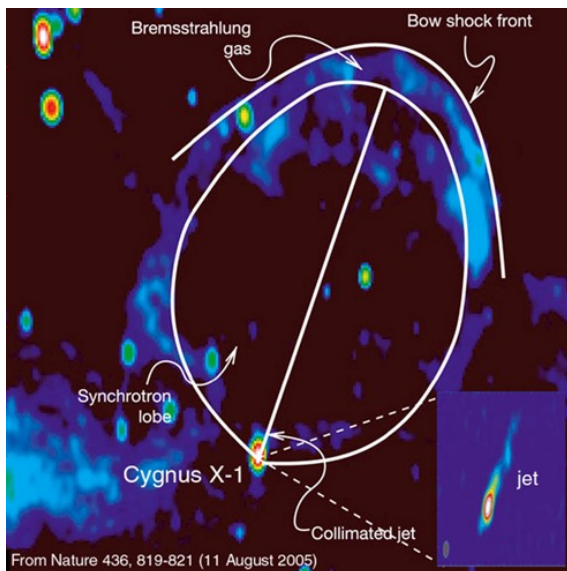


Figure 1.1: A observation (from Gallo et al., 2003) of the bubble around Cygnus X-1 at 1.4 GHz with descriptions of the components. The ring-like structure has a diameter of around 5 pc. The insert shows the inner radio jet.¹

origin in the potential energy of the gas falling in the black hole. The potential energy in the infinite is decreased while the gas is falling in the black hole and this released energy is heating the accretions disc and is emitted as radiation. This radiation should be situated in the X-ray region (Karttunen et al., 2007).

The behavior of stellar black holes in binary systems is similar to the behavior of active galactic nuclei (AGN)(Uttley et al., 2002, 2005). AGN are super massive black holes in the center of whole galaxies. We know them as e.g. quasars and many of them have accreting discs and jets (Karttunen et al., 2007).

The difference between a black hole in a binary system, often called mircoquasar, and the AGN is the mass scale (e.g. Fender, 2010; Markoff, 2010). AGN have million times the mass and therefore dimensions of a stellar black hole. This causes the difference of time scales for similar processes. So AGN allow to study small time scales and short changes of the accreting process and stellar black holes like Cygnus X-1 allow the study of very long time scales in this process. This makes the easily observable object Cygnus X-1 a great example to study the accreting and the jet mechanisms of both stellar black holes in binary systems and AGN.

1.2.2 Accretions Process

The blue super giant star HDE 226868 has a loss of $\dot{M} = (2.57 \pm 0.05) \times 10^{-6} M_{\odot} y^{-1}$ (Gies et al., 2003) and its wind has a terminal velocity of 2100 km s^{-1} which can provide material for the accretion disc of Cygnus X-1. Also the star is close to filling its Roche lobe. The wind is strongly focused towards its companion and is highly asymmetric (Friend & Castor, 1982). This accretion disc has great evidence. The soft state has a spectrum that can be well described by a thermal emission a standard accretion disc would emit (Wilms et al., 2006). Any hard spectral components in the soft state do not show any appreciable curvature up to the MeV regime (Grove et al., 1998; McConnell et al., 2000, 2002).

1.2.3 The Jet

There are also jets, collimated outflows, of matter accelerated to the relativistic speeds which often appear at accreting systems such as binary systems or AGNs. Jets of microquasars were already observed and imaged in the radio (see Gallo, 2010, for an overview of such observations).

¹source of the figure <http://www.nature.com/nature/journal/v436/n7052/full/nature03879.html>



Figure 1.2: *An artistic illustration of Cygnus X-1 by David A. Hardy*³

And for jets of AGNs whole projects have been established to observe them².

For Cygnus X-1 there is also evidence of a jet. Stirling et al. (2001) have imaged a jet-like structure in radio observations. In Fig. 1.1 a image of a radio observation of the jet of Cygnus X-1 is shown and also a large scaled bubble of the interaction between the jet and the interstellar medium. For better imagination how the system may look like Fig. 1.2 shows a artistic illustration of a binary system.

1.2.4 Hard and Soft State - the q-Track

The last important thing to know for this work is how the observed information from such an object as Cygnus X-1 can be characterized. The distinct radiation regimes that could be occupied, so-called states, are defined by the spectral features and the timing properties (Fender et al., 2009; Belloni, 2010). With the hardness-intensity diagram (HID) shown in Fig. 1.3 the different shapes of spectral features and the timing properties are brought into a diagram. In this diagram the X-ray luminosity is plotted against the hardness of a source. The Hardness is the quotient of two defined energy bands first the hard band and then the soft band. So if there are much hard photons compared to the soft ones the hardness is high. This parameter can be compared with the Γ parameter of a power law describing the shape of the spectra, but for a high hardness the Γ has low values and vice versa.

The Hard State (LHS for Low Hard State) shown in the Fig. 1.3 has a Γ lower than 2, so the source is bright in the hard X-rays compared to the soft X-rays and the spectrum has a flat shape. Also there is a correlation between radio, IR and X-rays and a compact jet can be resolved in radio observations for some sources. When a source get brighter in this state it can change into the Hard Intermediate State (HIMS) and its hardness drops. So the Γ increases over 2 and it crosses the Jet Line Area (JLA) to the Soft Intermediate State (SIMS) and then reach the Soft State (HSS for High Soft State). In the HSS there are often radio flares and the shape of the spectra is described good with a non-thermal power law up to MeV. In this state there are less high X-ray emissions as in the LHS. The combination of the states between the

²For example the Tanami Project <http://pulsar.sternwarte.uni-erlangen.de/tanami/>

³source <http://spaceart1.ning.com/>

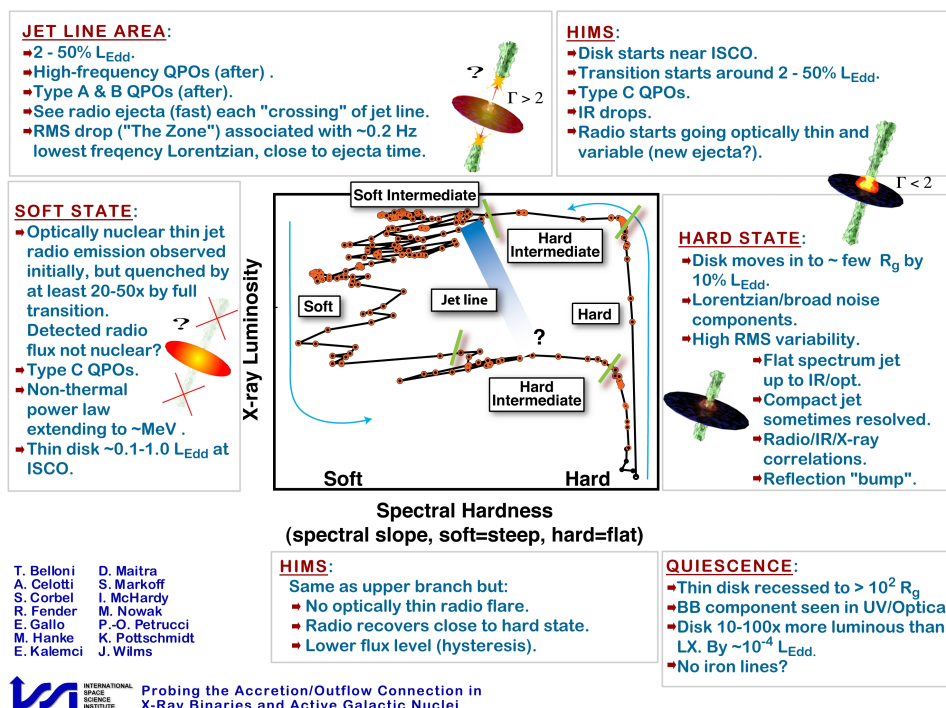


Figure 1.3: The so called *q-Track*, the current idea of the states of black hole binaries. Short descriptions of the different states are included in the figure⁴. Abbreviations: quasi periodic oscillations (QPOs), innermost stable circular orbit (ISCO)

LHS and the HSS is later called the transitional state. The states also show different timing properties, but they are not discussed here because they are not necessary for this work.

The Fig. 1.4 shows also a schema of the hard and the soft state. For more Information and descriptions see Grinberg (2010). Cygnus X-1 was between 1996 and 2004 only 4 percent in the HSS, 21 percent in the transitional state and mostly in the LHS with 75 percent of the time (Wilms et al., 2006).

⁴source <http://www.sternwarte.uni-erlangen.de/proaccrretion/>

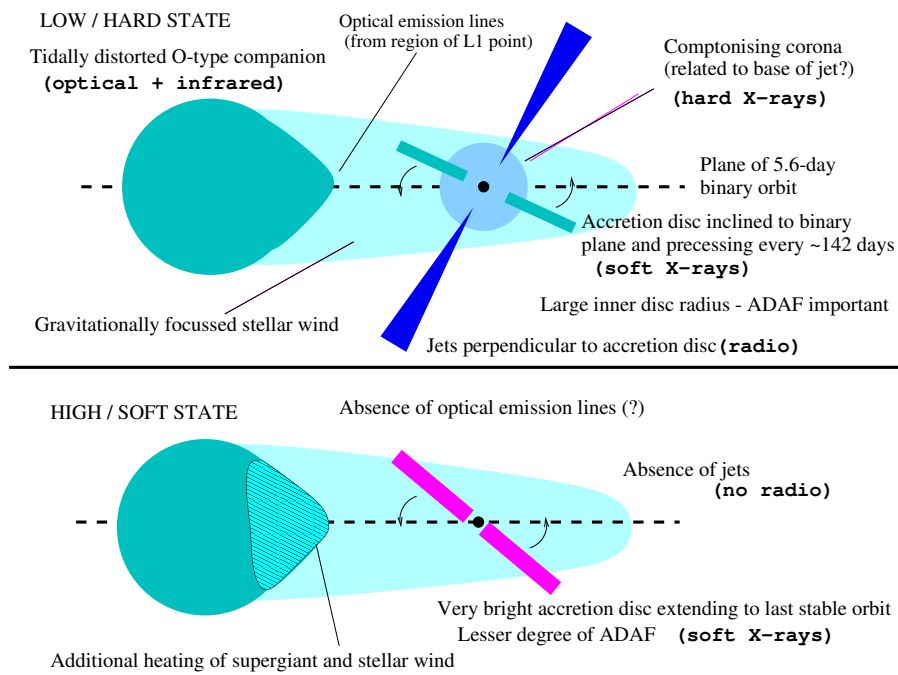


Figure 1.4: *The hard and the soft state and how it could look like in this state (Brocksopp et al., 1999)*

Chapter 2

Methodes of Observation

2.1 High Energy Observations

The atmosphere is only in a few wavelength ranges transparent to the radiation. The Fig. 2.1 shows this dependence and for high energy astronomy there is no way to observe from the ground. So satellites are needed to observe high energy photons to make science with the information transported by the X-rays and gamma rays.

Another problem is the fact, that this high energy photons can not be collected and focused easily like photons in the optical range. There are telescopes to make X-ray images with total reflection called Wolter telescopes. With this technique photon energies up to 10 keV can be detected (Chandra X-ray Observatory). But on higher energies (above ~ 30 keV) this is not possible, the critical angle of the total reflection is extreme small and so there is now way to focus that photons with mirrors (see Fürst, 2010, for the calculation). So there have to be another way to make images in the highest energies.

The coded mask method can do this. In this technique the photons are not collected or focused, but they are filtered by a cover plate with specific placed holes in it called the coded mask. The photons pass through the holes or are blocked by the opaque elements of the mask. So every source casts a shadow of the mask on the detector plane below. The design of the mask has to be chosen in such a way that the combined shadows of the sources in the field of view has the information of all the single shadows (in't Zand, 1992). The principle of the coded mask is illustrated in Fig. 2.2.

To generate a picture of the sky in the field of view the detected information has to calculated back to the origin picture by using the unique design of the coded mask.

2.2 INTEGRAL Satellite

The **INTE**rnational **G**amma-**R**ay **A**strophysics **L**aboratory (*INTEGRAL*) is an ESA project and the satellite was launched on October 2002. Its on an elliptical orbit around the earth with a period of 72 hours and maximum distance of 153600 km. This and the information in the next few paragraphs can be found on the official *INTEGRAL*-webpage (<http://www.sciops.esa.int/index.php?project=INTEGRAL>).

The satellite consists of two main gamma-ray instruments, the spectrometer SPI and the imager IBIS. This two instruments work both with coded mask method and complement each other, the design of SPI is optimized for high resolution spectroscopy with an low spatial resolution and on the other hand the IBIS instrument is optimized to imaging of point sources with a big

¹source <http://www.ipac.caltech.edu/outreach/Edu/Windows/irwindows.html>

²source http://www.sciops.esa.int/index.php?project=INTEGRAL&page=About_INTEGRAL_Instruments

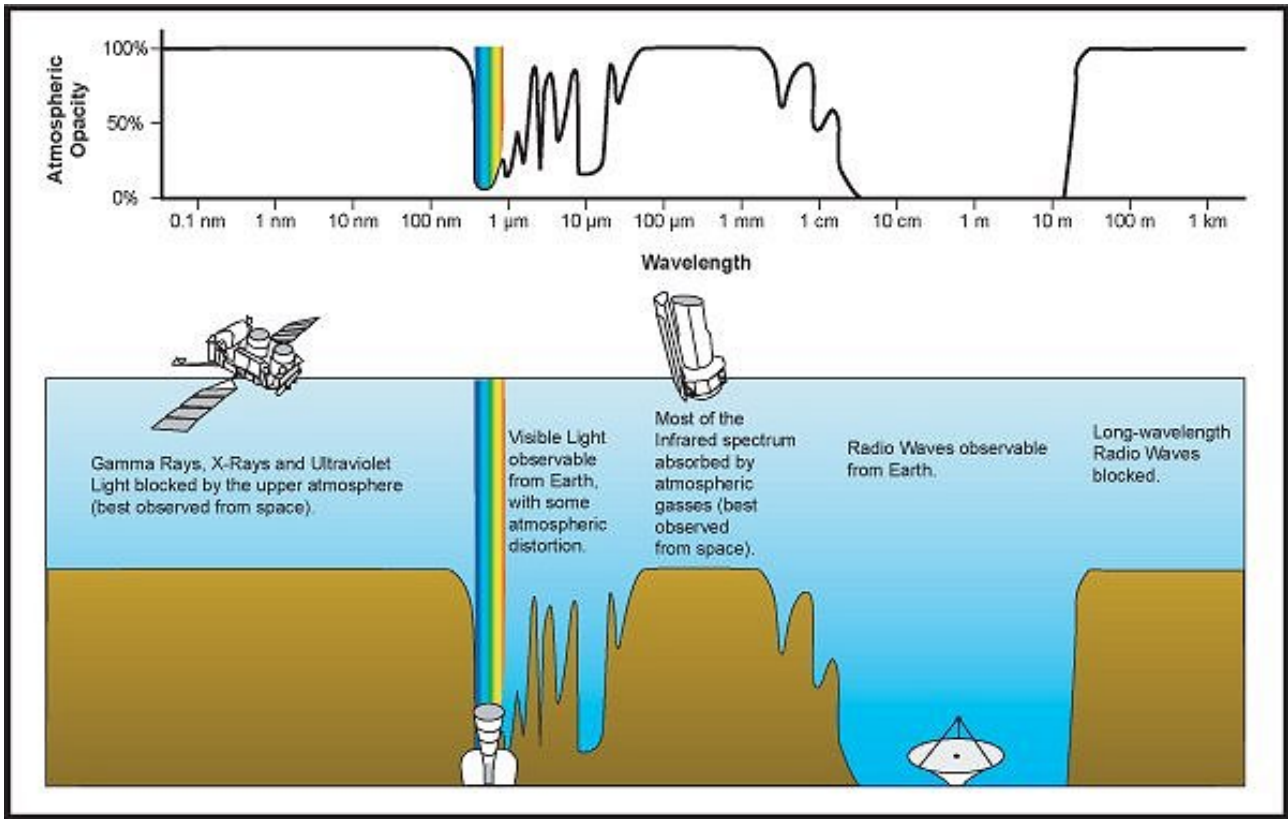


Figure 2.1: *The atmospheric absorption of the radiation depending on the wavelength¹*

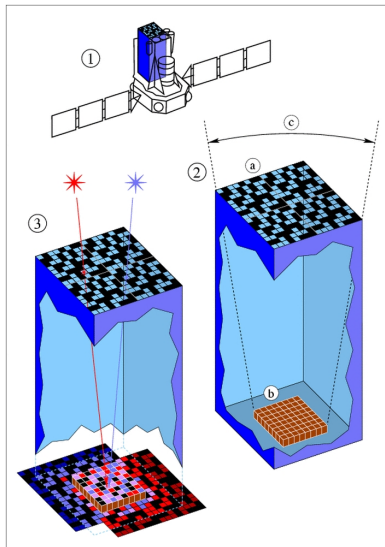


Figure 2.2: *The principle of the coded mask. The cover plate (a), the position of the detector layer (b) and the field of view (c) are marked in the schema. In this example two (red and blue) sources cast shadows of the mask in the detector plane and with this information the images can be reconstructed.²*

spatial resolution and only a moderate spectral resolution. The energy range of SPI is from 18 keV up to 8 MeV and of IBIS from 15 to 1000 keV with maximum effectiveness between 20 and 100 keV.

The IBIS instrument consists of two different detection layers, the upper layer is the ISGRI detector which is mainly used for this work and has a sensitive area between 15 and 1000 keV. The bottom layer is the PICsIT detector which is sensitive in the range from 100 keV and 10 MeV. With both layer its possible to reconstruct the angle of incidence of the photons.

There are also support instruments on *INTEGRAL*. The Joint European X-Ray Monitor (JEM-X), also a coded mask instrument, is present twice on the satellite and this two instruments help with the detection and identification of the gamma-ray sources and play also a role in the analysis and the scientific interpretation of the collected data. Their energy range is

from 3 to 35 keV. The two JEM-X instruments together with the ISGRI detector are the data sources for this work.

Furthermore there is an optical instrument on the *INTEGRAL* satellite the Optical Monitoring Camera (OMC). It observes the emission from the prime targets of the main instruments. The whole satellite with the described instruments is shown on the Fig. 2.3.

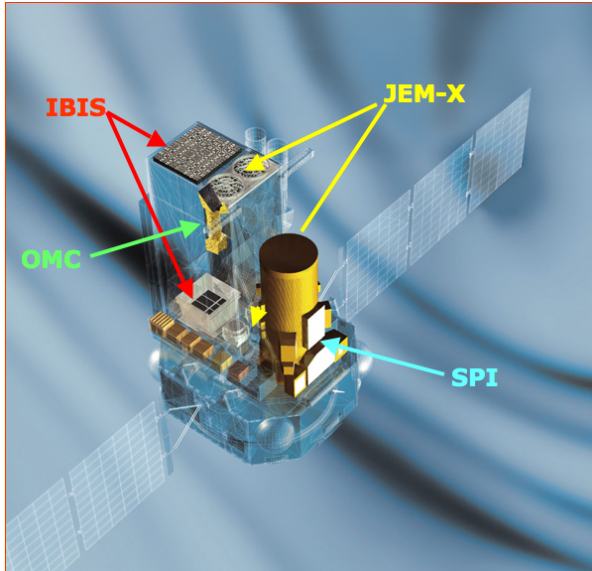


Figure 2.3: *The INTEGRAL Satellite with its instruments*³

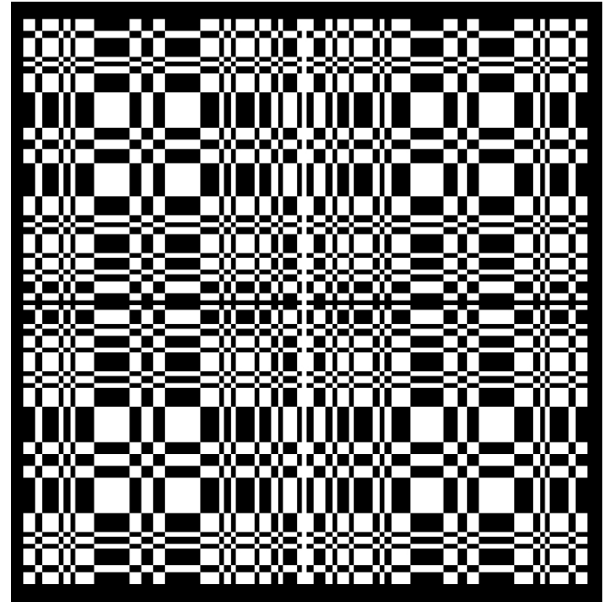


Figure 2.4: *The coded mask of the IBIS instrument on the INTEGRAL satellite (Chernyakova & Neronov, 2010)*

The figure 2.5 shows an artistic picture of Cygnus X-1 in the background and the different views of the described instruments of the source in the foreground. As it can be seen in the figure the instruments IBIS, JEM-X and SPI work with the coded mask method.

³source http://www.sciops.esa.int/index.php?project=INTEGRAL&page=About_INTEGRAL_Instruments

⁴source <http://sci.esa.int/science-e/www/object/index.cfm?fobjectid=32700>

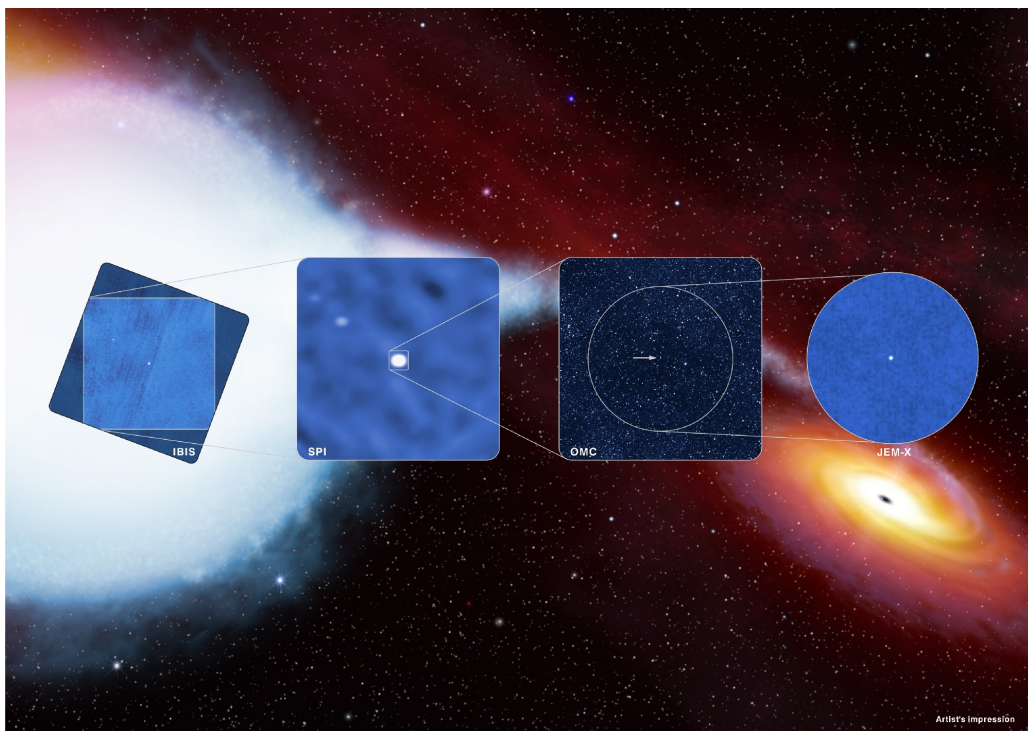


Figure 2.5: *INTEGRAL's view of Cygnus X-1*⁴

Chapter 3

Data Reduction

From this chapter on there will be some shortcuts which will be explained now. The *INTEGRAL* satellite observes the sky in revolutions of about 72 hours (short Rev) and there are up to hundred Science Windows (short ScW) in one revolution which are observations of about 30 minutes.

The revolutions of interest for this thesis are all done from August'10 to March'11. A total of 14 revolution are available, Rev0928 and Rev0938 were in the transitional state and Rev0983 to Rev0998 were in the soft state.

3.1 IBIS

Due to the fact, that the IBIS instrument on *INTEGRAL* is a coded mask instrument, the extraction and the analysis of the data is highly complex. And also it is not possible to work only with one source, the whole field of view has to be taken into account. Any source in the field affecting the others and the background.

The software used to extract and to create the images, light curves and spectra is the Off-line Science Analysis (OSA) software, of which we use the version OSA 9 for this thesis, the most actual currently available version of OSA. The single steps through the analysis follow the Cookbook Chapters of IBIS Analysis User Manual and JEM-X Analysis User Manual which both can be found on the ISDC web page¹.

The overall way to extract the data is to make first mosaics (images of the field of view), checking them and, after creating catalogs of found sources in them, proceed to make spectra of the ScW.

3.1.1 Images and Mosaics

Before starting to extract images, the first thing to do is finding the right revolutions and ScW with Cygnus X-1 in them. The small script OBJSCW provided by I. Kreykenbohm (priv.comm.) displays the available ScW where the given object is in the field of view of the IBIS or JEM-X instruments and report which of this ScW are available on the server of the institute Sternwarte Bamberg. By setting the maximum distance of Cygnus X-1 to the center of the field of view to 20 degree the script returns a list of the ScW needed for this work. With this list the extraction can start.

With the `og_create` program a so-called *observation group* has to be created as the first step of the IBIS data analysis. The cookbook of the IBIS Analysis User Manual suggest to create an observation group for all the ScW which will later be used to create the mosaic image and

¹<http://www.isdc.unige.ch/integral/analysis>

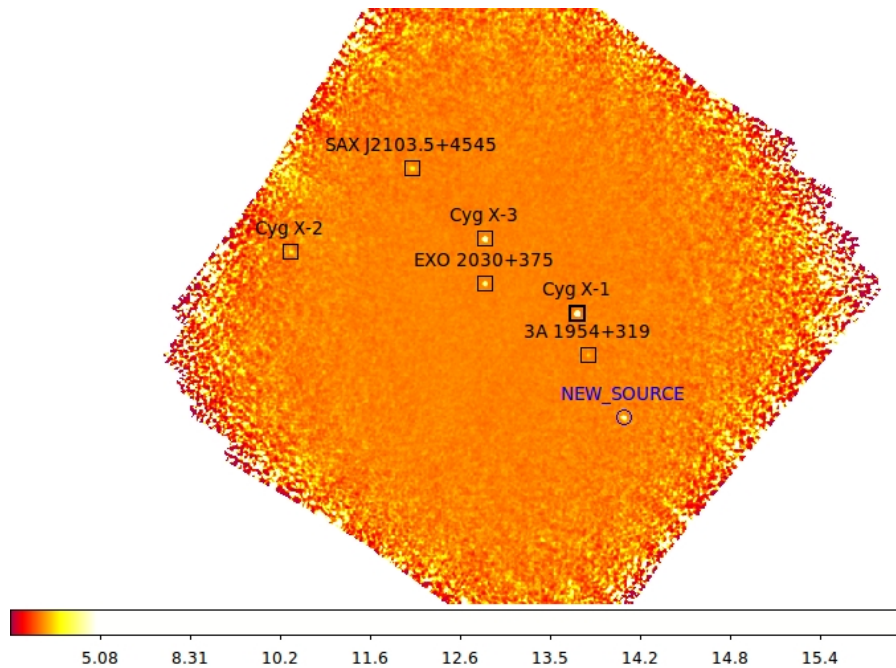


Figure 3.1: Mosaic of the revolution 0992 in the energy band from 20 to 40 keV

the combined spectrum. But for more flexibility in the future analysis every single ScW got its own observation group. This change means that mosaics and summed spectra need to be done in extra steps combining ScWs from different observation groups as explained in Sec. 9.4 of the IBIS Analysis User Manuals (Chernyakova & Neronov, 2010).

To generate the image for a single ScW the script `ima_sbs`² created by I. Kreykenbohm (priv.comm.) is used. After that a mosaic out of all single ScW in a revolution is created and with this mosaic the data can be checked to verify the right parameters in the data reduction in order to have the best result. Questions like how many sources are in the field of view and how bright are they compared to the primary source can be answered and incorporated into the analysis of the data.

One of this mosaics is shown in the Fig. 3.1. Cygnus X-1 as well as other X-ray sources can be seen on the mosaic and also an artificial source generated during the reconstruction of the sky. This is shown as a circle with the description `New_Source` in the Fig. 3.1. With a catalog of all X-ray sources the sources in the mosaics can be identified. A new catalog with only the detected sources created for each revolution is necessary for the extraction of the spectra. In this step only bright sources get in the new catalog, sources with a signal to noise below 6.0 do not receive attention. This weak sources influence the bright sources only marginal and the CPU time of the extractions is greatly reduced without the weak ones. Also the artificial sources need to be removed from the catalog.

3.1.2 Spectra

Due to the technique of the coded mask it is not possible to extract spectra for only one source in the field of view. All sources kept in the individual catalogs of each revolution will be considered in the spectral extraction.

With the script `spe_sbs`, also created by I. Kreykenbohm (priv.comm.), one spectrum for every

²Later to deal with the large amount of data (over 900 ScW from ISGRI only) the script `master_sbs` created by I. Kreykenbohm (priv.comm.) was used, because it creates jobs using `mosa_sbs` and `ima_sbs` out of a list of ScW for mosaic and spectra creation which are processed by the cluster of the Data Center of FAU University Erlangen-Nürnberg.

ScW was extracted. In this process the specific catalog created after the mosaic step is needed as well as the response files which will be described later in Sec. 5.

The individual spectrum of each ScW is stored in the file `swg_ibis.fits` located in a sub folder of the observation group. With tool `spe_pick` and the steps also described in the Sec. 9.4 of the IBIS Analysis User Manuals (Chernyakova & Neronov, 2010) the spectra were summed to one spectrum for every revolution.

The figure 3.2 show the summed spectrum of the revolution 0998 without any additional reduction or editing. For the later following analysis there were additionally created a summed spectrum for the revolution 0983 to 0989 and 0992 to 0998, explained in Sec. 5.3, and also one over all revolutions in the Soft State (Rev0983 to Rev0998). This spectra are now ready to be fitted with models using the `ISIS` tool described in Chapter 4.

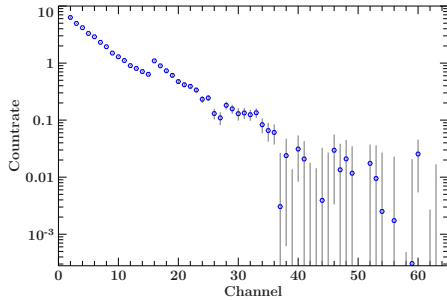


Figure 3.2: *Raw spectrum of the revolution 0998 as observed by ISGRI*

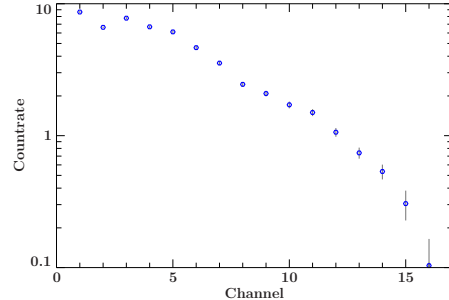


Figure 3.3: *Raw spectrum of the revolution 0988 as observed by JEM-X*

3.2 JEMX

The JEM-X data consists out of less ScW than the IBIS data because of the smaller field of view, so it is needed to make an extra list of ScW for this extraction. The Steps of data reduction follow the same schema as for IBIS and are described in the Cookbook of the JEM-X User Analysis Manual (Chernyakova et al., 2010).

The ScW also put in single observation groups and the scripts `ima_sbs` and `spe_sbs` are also used. But it is needed a special parameter for JEM-X extraction, the parameter `nChanBins` has to be set to -4 described in the cookbook³. Since there are two JEM-X instruments the extraction has to be done twice, i.e. for each instrument. To extract the spectra of the JEM-X data another response file is needed and also one catalog with only Cygnus X-1 in it for all revolutions. There is no need for a catalog for each revolution because there are no other source in the field of view of JEM-X bright enough to be detected by JEM-X. The figure 3.3 shows the summed spectrum of one of the revolutions.

³During this process the fluxes were extracted in $2^{-nChanBins}$ bins. The value -4 results in a production of 16-channel spectra. See Chernyakova et al. (2010) for more information.

Chapter 4

Summary of all available Data

4.1 Data Overview

After the image extraction of the IBIS and JEM-X instrument it is possible to compare the count rates in the individual energy bands with the count rates of other astronomical devices observing Cygnus X-1.

The data of the Monitor of All-sky X-ray Image (*MAXI*) mounted on a Japanese Module of the ISS can be downloaded on the official *MAXI* web page¹. This instrument has an energy range of 2 to 20 keV. Another source of data for Cygnus X-1 is the Burst Alert Telescope (*BAT*) on the NASA satellite *Swift*. It has the energy range of 15 to 150 keV² and the count rates from 15 to 50 keV are already on the server of the institute Sternwarte Bamberg. The last comparative data are from the Arcminute Microkelvin Imager (*AMI*), two radio telescope arrays whose bandwidth is centered at 15 GHz³. This Data also can be found on the local server. The figure 4.1 shows all the data from the external instruments and from the data reduction described in Chapter 3. It is split in two sides with a gap between the revolution ranges. That is because there is no data of *INTEGRAL* available between the two revolutions 0929 and 0938 and the other revolutions (0983 and higher) and so the single data points can be identified better in this plot.

In the revolutions of the soft state above 0980 the radio data from *AMI* are mostly equal to zero. The detections in energy bands higher than 7 keV show lower counts in the soft state (right side) as in the transitional state (left side) as expected. Also the count rates at lower energies increases as expected in the soft state.

4.2 A Closer Look

There are some areas of the Fig. 4.1 that show great analogy of the data of the different instruments. The first eye-catching area is shown in the left plot of Fig. 4.2. The higher energy band of both JEM-X instruments (blue points) have a structure clearly similar to the structure of data points of the lower energy band of the ISGRI instrument of IBIS (red points). The same behavior can be seen in the middle plot of the Fig. 4.2. The major difference between the structure of the data points in the energy band 7 to 20 keV (JEM-X) and 20 to 40 keV (ISGRI) is that ISGRI has more data points in the same interval than JEM-X.

In the right plot of the mentioned figure there is another behavior. The radio data from *AMI* has a burst of flux in the highlighted section and till 55521 MJD it falls back to zero. While this

¹<http://maxi.riken.jp/top/>

²<http://heasarc.nasa.gov/docs/swift/swiftsc.html>

³<http://www.mrao.cam.ac.uk/telescopes/ami/>

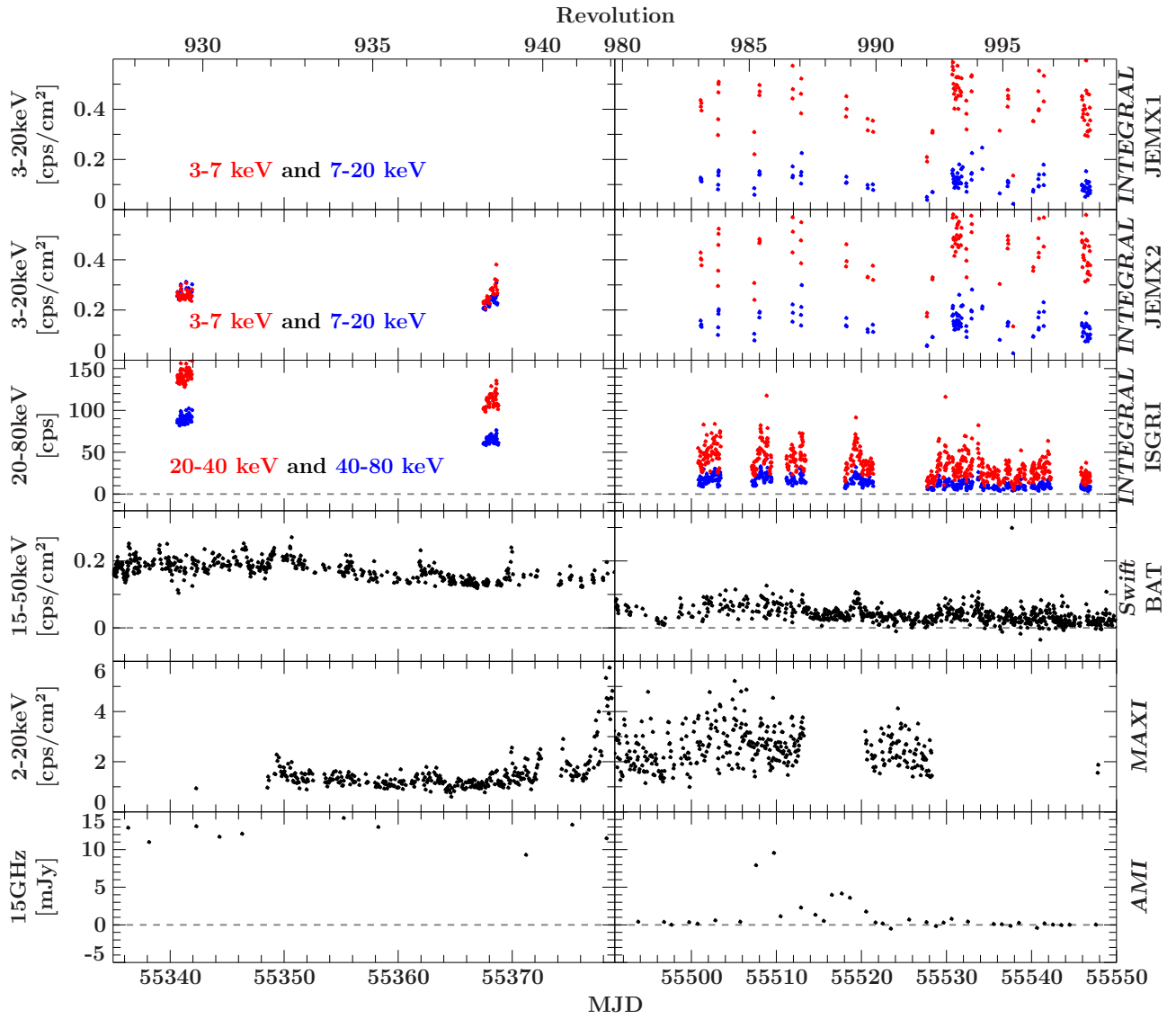


Figure 4.1: Flux in different energy bands and split in two revolution ranges

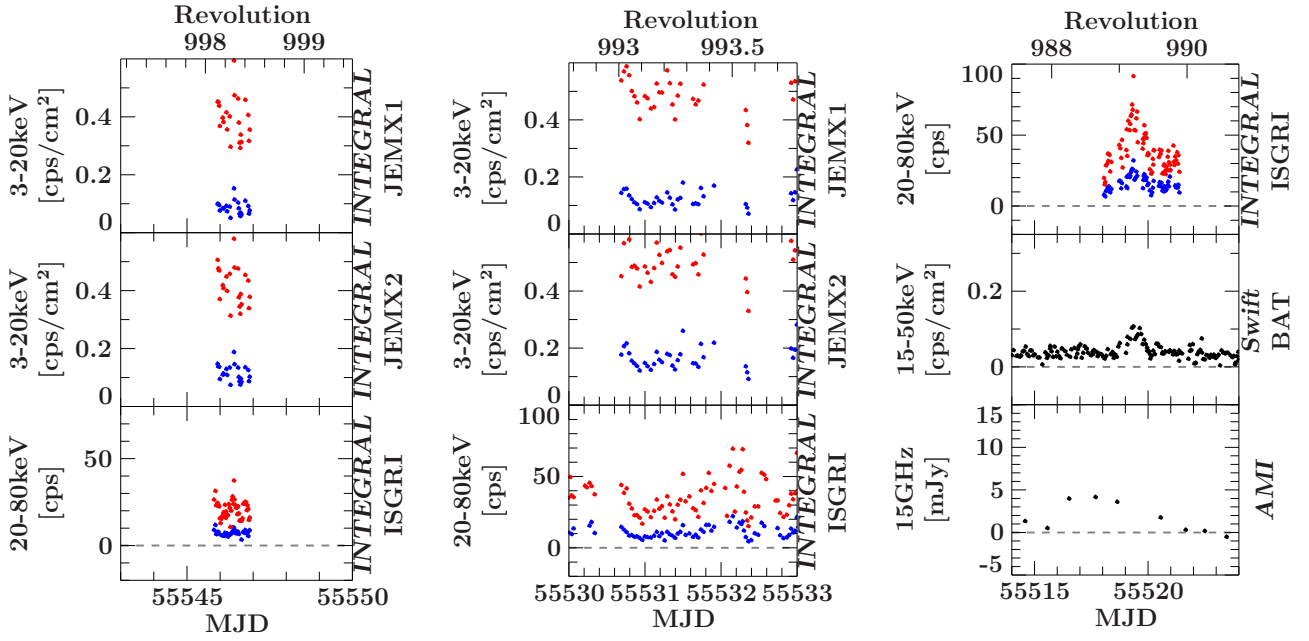


Figure 4.2: A closer look on details of the overview of all data as presented in Fig. 4.1

flux decreases the data of *Swift* BAT and ISGRI has also a burst in the count rate (around 55519 MJD). Data from the other instruments are unfortunately not available in this period.

Chapter 5

Spectral Analysis

After the overview of the available data reduced for this thesis and from other astronomical devices in this chapter data from ISGRI and JEM-X will be analyzed to learn more about Cygnus X-1 in the soft state.

5.1 Spectral Analysis Basics

But first of all it is necessary to understand how the details of the analysis work and what the later mentioned things are. This section will give a short overview of the way how to get useful data out of the raw data of the reduction.

In the raw data there are only count rates given per channel of the detector. This has to be connected to the spectral energy distribution (SED) from the source. The details of this behavior are described by Davis (2001). The SED is calculated from the count rates via two matrices. The first matrix is the response function (RMF), which is the same for all INTEGRAL observations, and the second matrix is the effective area or ancillary response function (ARF), which is time-dependent. The ARF is the variable part of the calculation and reflects the changing accuracy of the detectors of the IBIS and JEM-X instruments. This two files have to be available during the extraction and the analysis of the data (Hanke, 2007).

The program which is used in this thesis to analyze data is the **I**nteractive **S**pectral **I**nterpretation **S**ystem (software package ISIS) (Houck & Denicola, 2000; Houck, 2002). With this program the spectra can be scientifically treated and it is comparatively easy to add non-X-ray data. The fit functions described in the next section are available in the ISIS and the information is from the included help. This functions can be easily fitted to the data loaded in ISIS. Another advantage of ISIS is that it is possible to create own scripts for ISIS with the programming language **s-lang** to automate often used actions.

5.2 Fit Functions

In this section the functions used to fit the data will be introduced and their parameters explained.

- **powerlaw**

The **powerlaw** fit function is a simple photon power law with the parameters Γ the photon index and K [photons keV⁻¹ cm⁻² s⁻¹] the normalization factor.

$$A(E) = KE^{-\Gamma} \tag{5.1}$$

- **cutoffpl**

The **cutoffpl** fit function is like the **powerlaw** with an additional high energy exponential cutoff part. The extra parameter is the folding Energy E_{fold} of the cutoff in keV.

$$A(E) = KE^{-\Gamma} \cdot e^{-\frac{E}{E_{\text{fold}}}} \quad (5.2)$$

- **bknpower**

The fit model of an broken power law is called **bknpower**. The parameters are Γ_1 the power law photo index for $E < E_{\text{break}}$, Γ_2 the same for $E > E_{\text{break}}$, E_{break} the break point for the energy in keV and K the normalization factor [photons keV⁻¹ cm⁻² s⁻¹]. Γ_1 also called the soft power law index and Γ_2 the hard power law index.

$$A(E) = \begin{cases} KE^{-\Gamma_1} & \text{for } E \leq E_{\text{break}} \\ KE^{\Gamma_2 - \Gamma_1} \cdot \left(\frac{E}{1\text{keV}}\right)^{-\Gamma_2} & \text{for } E \geq E_{\text{break}} \end{cases} \quad (5.3)$$

- **compTT**

The **compTT** fit function is a analytical Comptonization model by Titarchuk (1994). It describes the Comptonization of soft photons in a hot plasma. The parameters are a normalization factor, the redshift frozen to value 0, the geometrical switch **approx** also frozen to value 1, the temperature of the input photons T_0 [keV], the electron temperature of the Comptonization plasma kT [keV] and τ_p as the optical depth¹.

- **highcut**

The **highcut** fit function is a high energy cutoff with E_c the cutoff energy and E_{fold} the e-folding energy both in keV.

$$M(E) = \begin{cases} \exp\left[\frac{E_c - E}{E_f}\right] & \text{for } E \leq E_c \\ 1.0 & \text{for } E \geq E_c \end{cases} \quad (5.4)$$

- **egauss**

Finally the **egauss** fit model is Gaussian line profile function with A [photons s⁻¹cm⁻²] the area under the curve, E_0 [keV] the center of the Gaussian curve and σ the width of it. This function is used as a model for the *Fe K α* emission line at about 6.4 keV

$$G(E_a, E_b) = \frac{A}{\sigma\sqrt{2\pi}} \int_{E_a}^{E_b} dE \exp\left[-\frac{(E - E_0)^2}{2\sigma^2}\right] \quad (5.5)$$

5.3 ISGRI

First of all the data of different summed spectra were load and fitted with the ISIS tool. The first step was to test the different fit functions how good or how bad they describe the data of the ISGRI instrument in the energy range from 20 to 500 keV. ISIS calculates automatically the right spectral energy distribution out of the raw data by using the given RMF and ARF. The data points were regrouped to have a signal to noise ratio of minimum 4.5 and a systematic error of 2 percent were added to the data (Chernyakova & Neronov, 2010). Also only data from 20 keV to 500 keV were taken into account for the analysis. The choice of the fit function is the empirical model **cutoffpl** and the **compTT** with its physical meaning.

¹Animated informations of the behavior of the parameters of the **compTT** can be found on the homepage of D.Maitra under <http://www.astro.lsa.umich.edu/~dmaitra/models/>

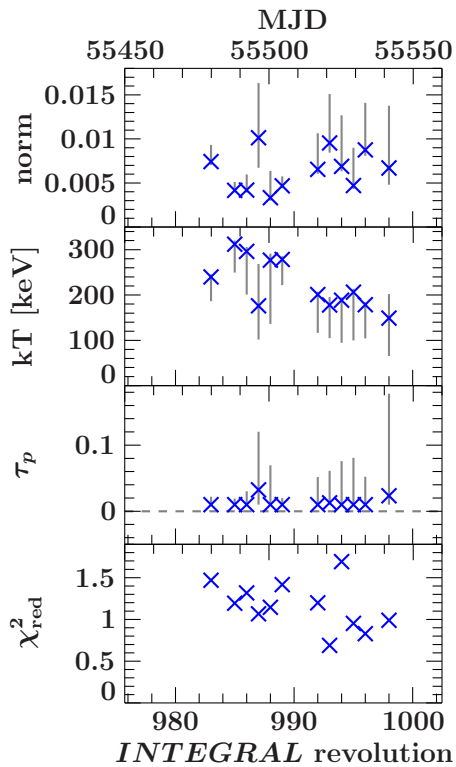


Figure 5.1: Parameters of the Comptonization model (blue crosses). Using the standard ARF. Parameter of the revolutions 0929 and 0938 are not shown due to a better clarity. Rev0929: $norm = 0.034$, $kT = 55.4$, $\tau_p = 1.04$, $\chi_{red}^2 = 1.50$; Rev0938: $norm = 0.027$, $kT = 61.0$, $\tau_p = 0.78$, $\chi_{red}^2 = 1.66$

Due to the information of the overall spectral evolution published by Grinberg et al. (2011a) how the parameters of the `cutoffpl` model behave in the soft stat, the E_{cut} is often badly constrained and takes on the maximal allowed value of 500 keV and the error bars nearly cover the whole allowed range, the simple `powerlaw` function is also used to fit the data.

In this process all the summed Spectra of each revolution were fitted by each of this three models and the parameters and the plot of the fitted spectra were saved.

5.3.1 First Results

The first results of the modelling of the spectra were the parameters of the models. All this parameters were saved during the fitting and analyzing and can be found in Appendix A in table A.1, A.2 and A.3.

In the Fig. 5.1 the best fit parameters are shown. One interesting feature in this fit parameters are the low values of the τ_p parameter. The most of them take on the minimal allowed value of 0.01, nevertheless the error bars of this parameter are small compared to the error bars of the higher τ_p values. The τ_p values of the both not shown revolutions are even higher, but this two revolutions are not in the soft state they are in the transitional state and therefore the higher values are expected.

A comparison between the parameters of the `powerlaw` and the `cutoffpl` model in the soft state is shown in the Fig. 5.2 and the best fit parameters are listed in the table A.1 and A.2 in the Appendix. The values of the photon index Γ are comparable for both models. The values of χ_{red}^2 are also comparable, with a possible trend for the `cutoffpl` model to describe the data very slightly better.

The values of the Γ for both models are the revolution 0983 to 0998 over 2 and this is expected in the soft stats (as explained Sec. 1.2.4 Fig. 1.3). For the transitional state revolutions these values are around 2 for the `powerlaw` model and lower than 2 for the `cutoffpl` model. This is also expected due to the change of the Γ in the transitional state from under 2 to values above 2.

Another feature recognizable in the Fig. 5.2 are the two flavors of the soft state where the

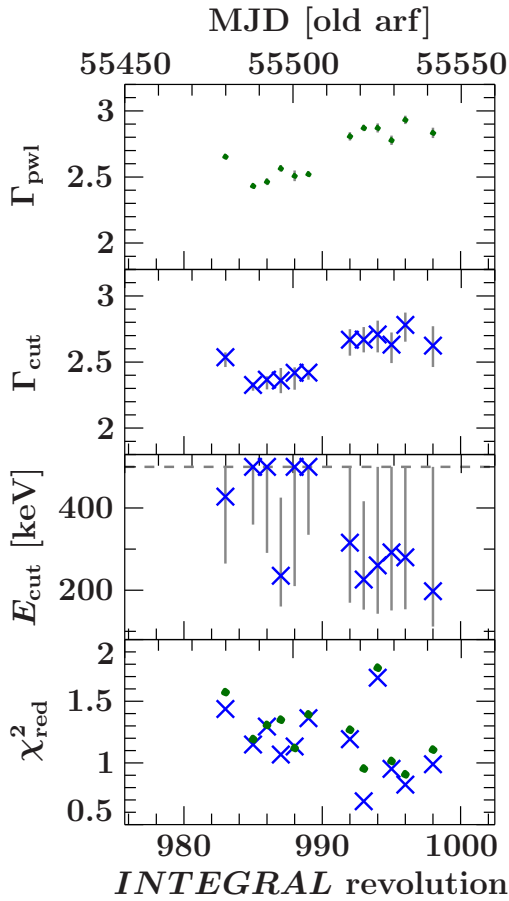


Figure 5.2: Parameters of the powerlaw (green dots) and the cutoff powerlaw (blue crosses) fit. Using the standard ARF. Parameter of the revolutions 0929 and 0938 are not shown due to a better clarity. Rev0929: $\Gamma_{pwl} = 1.945 \pm 0.009$, $\Gamma_{cut} = 1.52 \pm 0.03$, $E_{cut} = 176_{-13}^{+14}$, $\chi^2_{red,pwl} = 13.70$, $\chi^2_{red,cut} = 1.91$; Rev0938: $\Gamma_{pwl} = 2.050 \pm 0.010$, $\Gamma_{cut} = 1.68 \pm 0.04$, $E_{cut} = 190 \pm 20$, $\chi^2_{red,pwl} = 8.34$, $\chi^2_{red,cut} = 1.77$

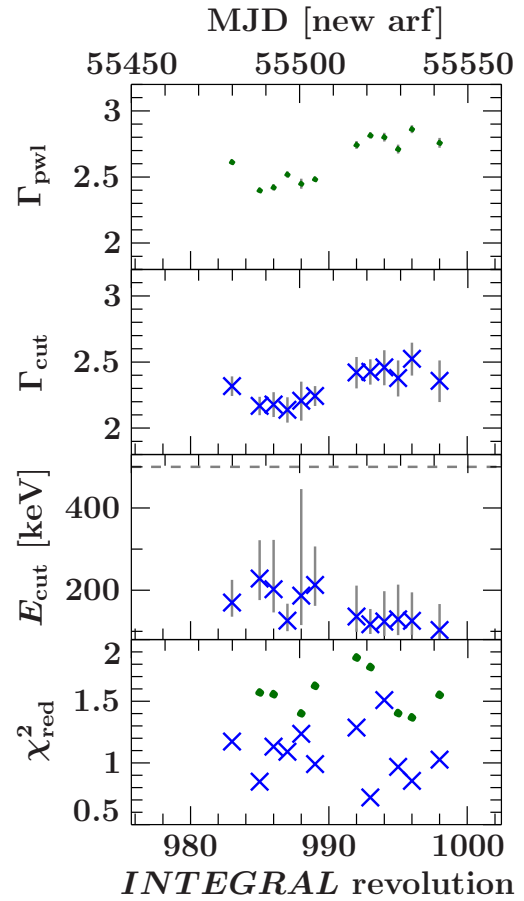


Figure 5.3: Parameters of the powerlaw (green dots) and the cutoff powerlaw (blue crosses) fit. Using the new ARF. Parameter of the revolutions 0929 and 0938 are not shown due to a better clarity. Rev0929: $\Gamma_{pwl} = 1.932 \pm 0.009$, $\Gamma_{cut} = 1.46 \pm 0.03$, $E_{fold} = 153_{-10}^{+12}$, $\chi^2_{red,pwl} = 13.54$, $\chi^2_{red,cut} = 0.48$; Rev0938: $\Gamma_{pwl} = 2.040 \pm 0.010$, $\Gamma_{cut} = 1.58 \pm 0.04$, $E_{fold} = 147_{-11}^{+13}$, $\chi^2_{red,pwl} = 9.66$, $\chi^2_{red,cut} = 0.79$

Γ_{pwl} are in two distinct regimes, which is also noticeable in the values of Γ_{cut} . The first group (Rev0938 to Rev0989) of Γ_{pwl} is around 2.5 and the other (Rev0992 to Rev0998) is around 2.9. The regimes of the flux counts of this two flavors also are different (2.1 to 3.9 $\text{keV s}^{-1} \text{cm}^{-2}$ and 1.1 to 1.2 $\text{keV s}^{-1} \text{cm}^{-2}$). During the first group there is an increased radio activity (see Chapter 4 Fig. 4.1). The radio flaring seems to be therefore coincident with spectral hardening within the soft state.

5.3.2 Search for the Hard Tail - Strange Residuals

Although both models fit well with the data, they show strong similar residuals between 50 and 100 keV, visible in not only in these two but also in the `comptT` model. In addition to that there is also a small excess in the first bin around 20 keV in all three models and almost all revolutions. To improve the shape of the residuals a few spectra combining several revolutions were extracted. Also there could be a hard tail (a non-thermal tail) seen in the higher energy ranges in the spectra as has been detected e.g. by Fritz (2008) and Cadolle Bel et al. (2006).

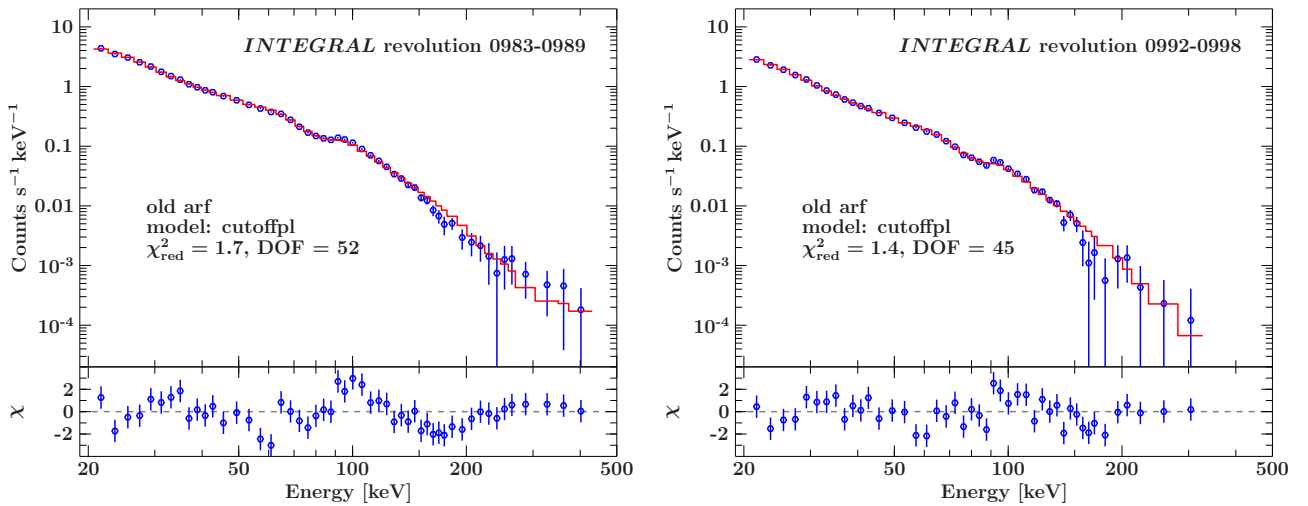


Figure 5.4: *The summed spectra of the revolution ranges Rev0983 to Rev0989 (left) and Rev0992 to Rev0998 (right)*

So by combining more revolutions there is the hope to see this hard tails even in this data of the soft state.

One spectrum with all available revolution and one without the transitional state revolutions (Rev0929 and Rev0938) were created. In addition to that there can be recognized two ranges of different flavors in the parameter values of the soft state, one from Rev0983 to Rev0989 and the other from Rev0992 to Rev0998. For each of this two flavors one overall spectrum were extracted. This new spectra were analyzed by the written scripts using the ISIS program.

The hard tails were not detected in this new summed spectra, this can be caused by the bad residuals, which drive the fit and outweigh the possible excess at high energies, and the low flux detected in the high energies.

The Fig. 5.4 shows two exemplary fits of the summed spectra over the two flavor ranges in the soft state. These plots were done for the poster (Grinberg et al., 2011b) of the conference "Black Hole Astrophysics: Tales of Power and Destruction" in Winchester in July 2011. Even with the summed spectra of the two flavors and also of the whole revolutions the residuals have this unique shape and small excess in the bin around 20 keV. Better fits were not achieved even with a combination of two power law components. Due to this behavior the calibration of the ISGRI instrument might be a reason and has to be assessed.

5.3.3 Assessing the Calibration Problems

Since the residuals of all the revolution fitted by the three different models have a similar look with very alike features in the same energy ranges in it and this behavior can be related to the change of the effectiveness of the ISGRI detector, which is not yet fully taken into account by the current ARF. This can be improved by using a more up to date ARF. (A not officially released testing version of the ARF for the next OSA version was provided by the calibration team (P. Laurent: APC, CEA/IRFU, Paris, France; J. Rodriguez: Lab. AIM, CEA-Saclay, priv. comm.). Note that this is a pre-released version and that results of the work done in this thesis might be used to change and improve it.) This new ARF will be tested and the possible improvement of the fits will be discussed in this subsection.

The new ARF (`isgri-osa90-smo-rev967.arf`) has to be assigned manually in the scripts written to analyze the data by fitting the spectra with the models. Like in the step before the parameters of the models and the plots were saved. The parameters can be found in the Appendix A table A.4, A.5 and A.6.

Comparison of the different arfs
model: compTT

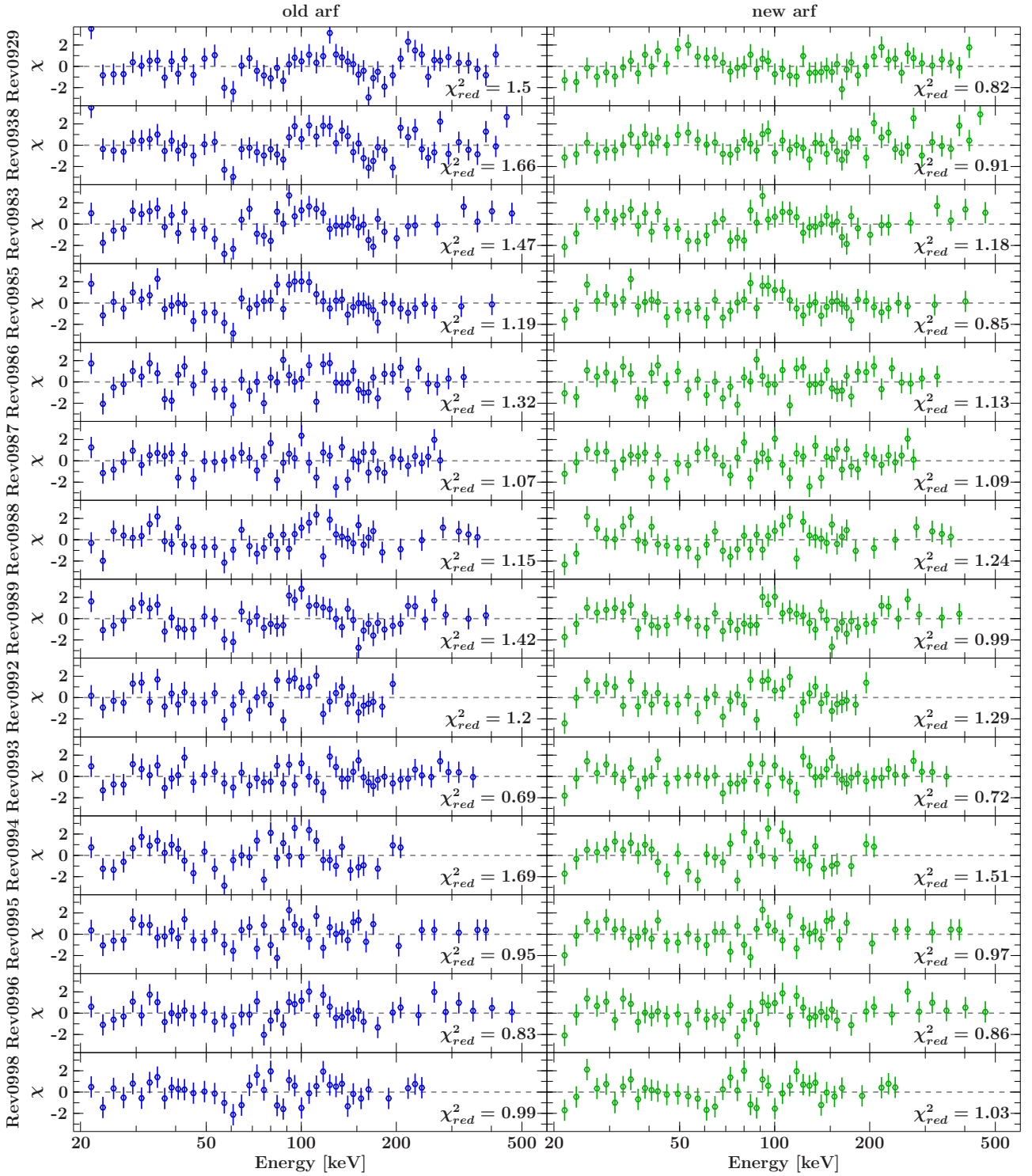


Figure 5.5: All residuals of the different revolutions fitted with the standard and new ARF (compTT model)

The plot in Fig. 5.3 is the same plot as in Fig. 5.2 however the new ARF is used. The Γ_{pwl} has almost the same values as before but the χ^2_{red} increased. The biggest change between the two plots are the improved values of the E_{cut} . Now with the new ARF they do not peg at the upper limit of 500 keV and the error bars are smaller, clearly showing the existence of a cutoff below 500 keV.

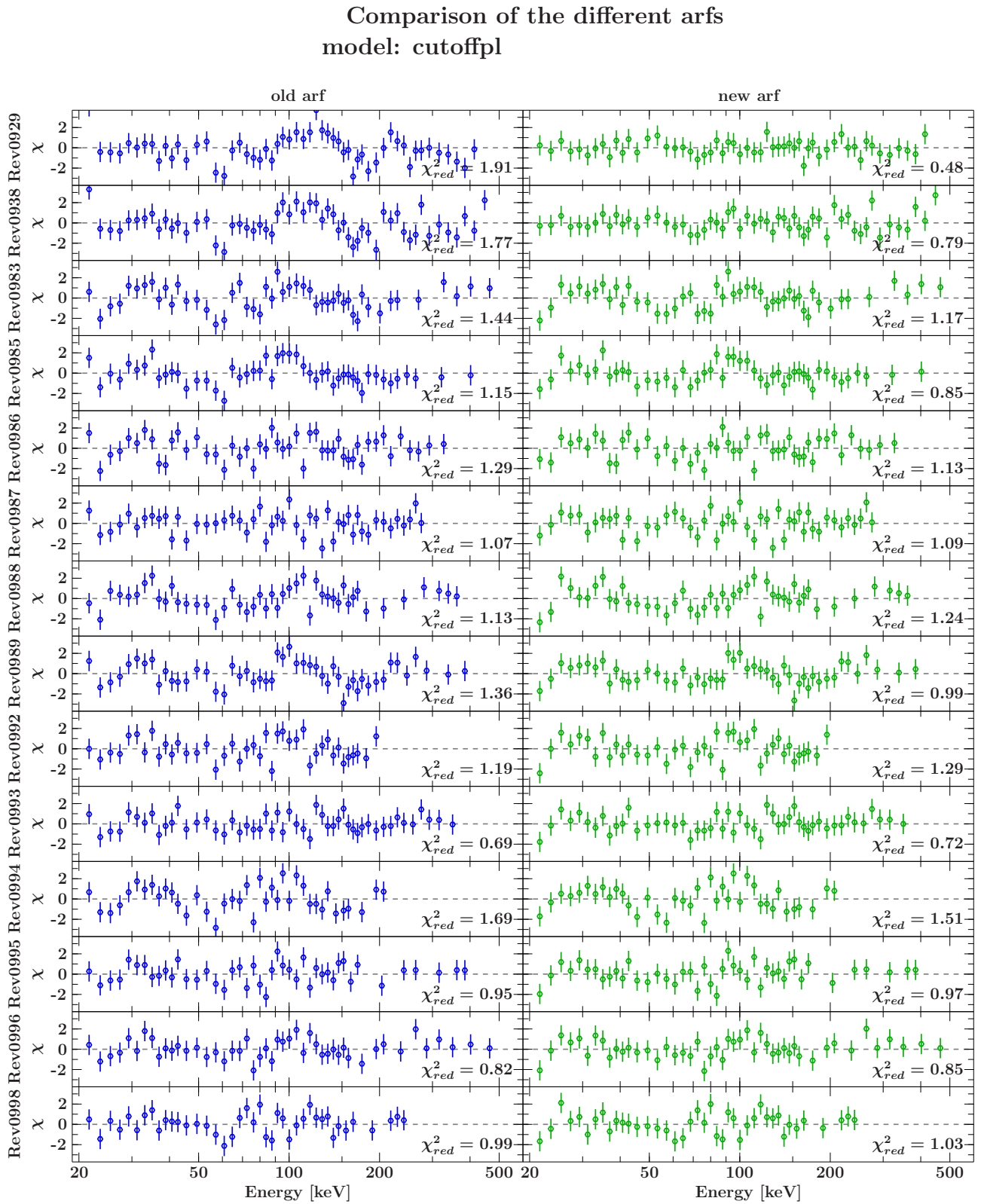


Figure 5.6: All residuals of the different revolutions fitted with the standard and new ARF (cut off pl model)

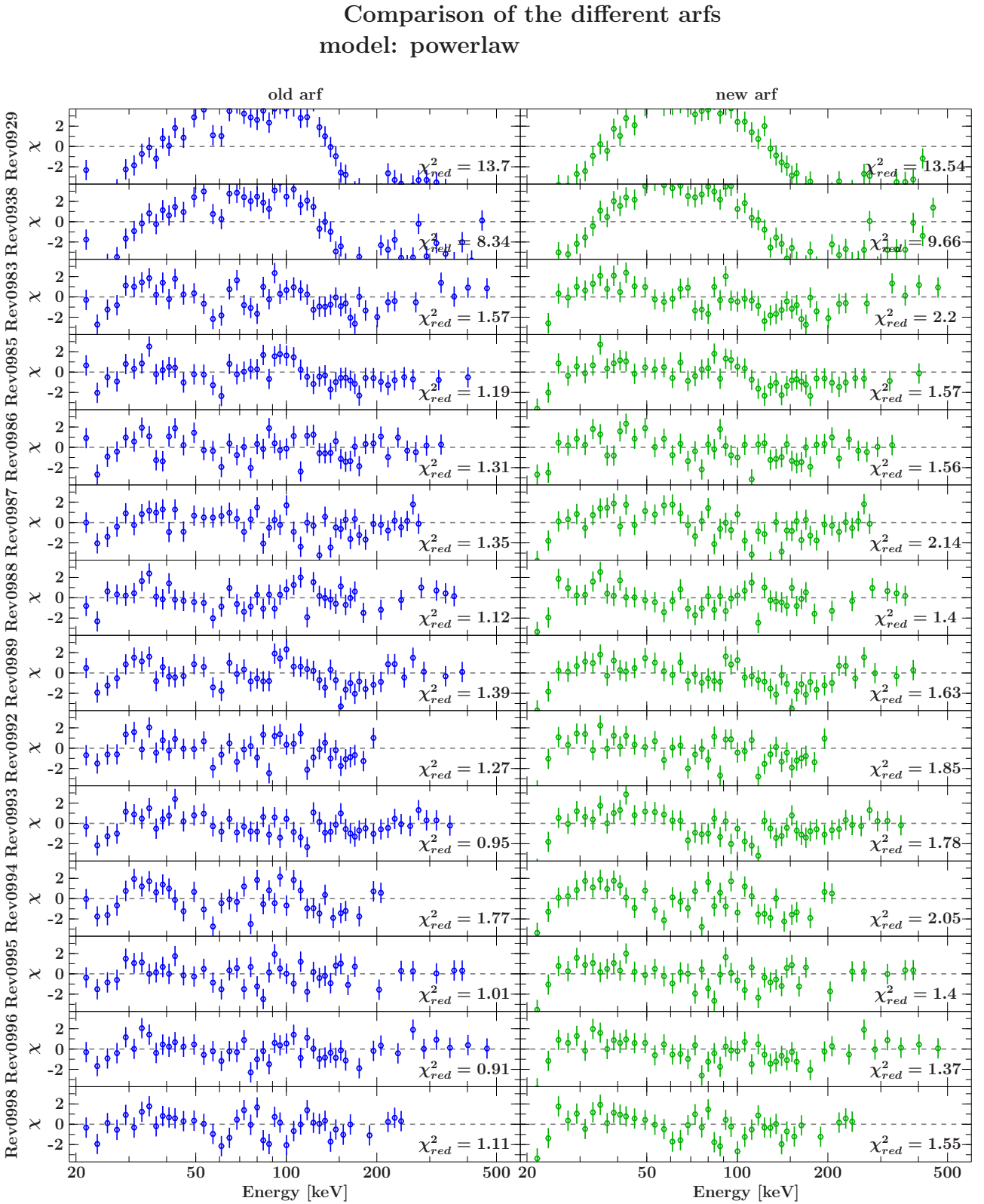


Figure 5.7: All residuals of the different revolutions fitted with the standard and new ARF (powerlaw model)

The Figures 5.5, 5.6 and 5.7 show the residuals of the different models with the standard (old) and the new ARF. Overall the `compTT` and most the `cutoffpl` model benefit from the new ARF, especially the first bin around 20 keV drops significantly. In the previous fits the models were systematically lower than this first data point. This effect changes and the models fit better with the data but for some revolutions the first bin is now significant lower than the models. So this changes of the first bins are not really good at all².

The most χ_{red}^2 of this models also drop and the shape of some residuals does not look so bumpy anymore. But in the different ranges of revolution the changes are also different in their strength. The revolutions of the transitional state benefit most from the new ARF, the first flavor of the soft state benefit slightly from it and the last revolution rang from 0992 to 0998 benefit only a bit or sometimes get worse than with the old ARF.

The simple `powerlaw` model does not benefit in the whole revolution range from the new ARF, but that's what is expected then the new ARF improves the calibration because the shape of the data should be more like a power law with a cutoff and not like only a power law. Only due to the bad constrained E_{cut} parameter of the `cutoffpl` model the `powerlaw` was used to fit the data. Especially for the soft state the power law model get with the old ARF χ_{red}^2 values comparable with those of the `cutoffpl` model and for the two revolutions in the transitional state the model do not fit great at all. After using the new ARF the $\chi_{\text{red,pwl}}^2$ get worse and $\chi_{\text{red,cut}}^2$ get better, so they are not comparable any more.

In conclusion the `cutoffpl` and the `compTT` model benefit from the new ARF and the `powerlaw` model do not fit well now, as expected then the new ARF works better than the old one. But it is not understood why only in a few revolutions the systematical shape in the residuals is gone and why it is not in the other revolutions. Also it is unclear why the first bin now sometimes deviates downwards from the models. This work done to test the new ARF will be used to improve the ARF and enable better working with the IBIS instrument in the future.

Another idea to improve the model fitting was to change the maximum angular distance of Cygnus X-1 to the center of the field of view of the ISGRI instrument, so Cygnus X-1 is in the fully coded field of view of the detector. The whole data reduction has to be done again with less ScW which were identified by the small script `OBJSCW` by using only 10 degree instead of 20 degree. After the same steps described above also for the new ARF the result of this test discovers that the whole residuals and χ_{red}^2 do not change noticeable (see Fig. 5.8 and also see all best fit parameter in the Appendix A in table A.7, A.8 and A.9). Only some small improvements can be found but also some worsening. The biggest disadvantage is the loss of many ScW through this new setting, around 300 ScW get lost.

Concluding the results, until a improved version of the ARF included in a new OSA version is released, the analysis of the data can go on with the old ARF and with a maximum angular range of 20 degree.

5.4 JEM-X

The data from the JEM-X instruments is in the energy range directly under the range of the ISGRI instrument, from 5 to 20 keV. The first step is to fit only the JEM-X data and then combine the JEM-X and the ISGRI data to fit them together. For the JEM-X data the `bknpower` and the `compTT` were chosen to fit the data. The `cutoffpl` model is not used to fit the data because the cutoff is out of the range of the JEM-X data and there is also a E_{break}

²The behavior with the first bin and the new ARF was communicated to the calibration team. They deal with this information and the new ARF hopefully work better, also to the fact that there is the same behavior with data from the crab nebula and pulsar (I. Caballero: Lab. AIM, CEA-Saclay, France, priv. comm.)

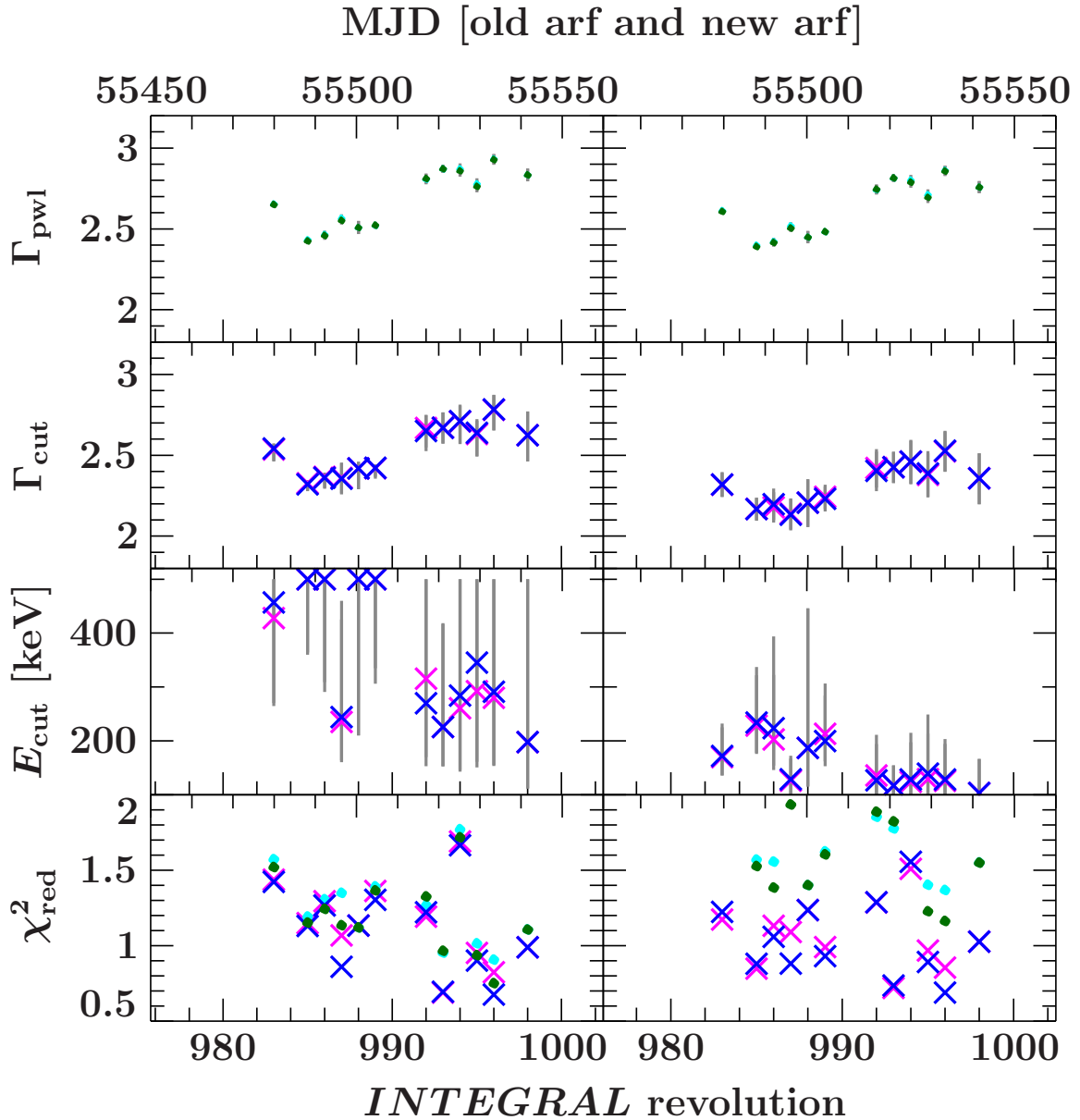


Figure 5.8: A comparison between the fit parameters of the data with 20 degree maximum angular distant with old and new ARF (power law model as green dots and cutoff plower law model as blue crosses) and same with only 10 degree (power law model as cyan dots and cutoff plower law model as magenta crosses). The Γ values and also the E_{cut} do not even change significant, only the χ^2_{red} values change slightly but do not get better overall.

of 10 keV which has to be taken into account (Wilms et al., 2006).

The data were grouped to have bins with a minimum signal to noise of 4.5 and also only the data from 5 to 20 keV were paid attention so there were only 8 bins left. Additional 5 percent of systematic error are needed for the JEM-X instrument.

The `compTT` model uses the same setting as in the ISGRI analysis and the `bknpower` models parameter E_{break} is set to 10 keV (Wilms et al., 2006). With this setting the residuals of the last model have an excess around 6 keV, i.e. there is an evidence of a Fe $K\alpha$ line in the spectra. By adding a `egauss` model with $E_0 = 6.4$ keV and $\sigma = 0.6$ (Wilms et al., 2006, have found parameters in this range in the RXTE fits) and a start value of 0.027 as the Area of the curve the `bknpower` model get better residuals without this feature. Because of the low quality of the JEM-X data the parameters, excluded the Area, of the Fe $K\alpha$ were frozen.

The fitting parameter of the `bknpower` model are shown in the Fig. 5.10. Both Γ parameter

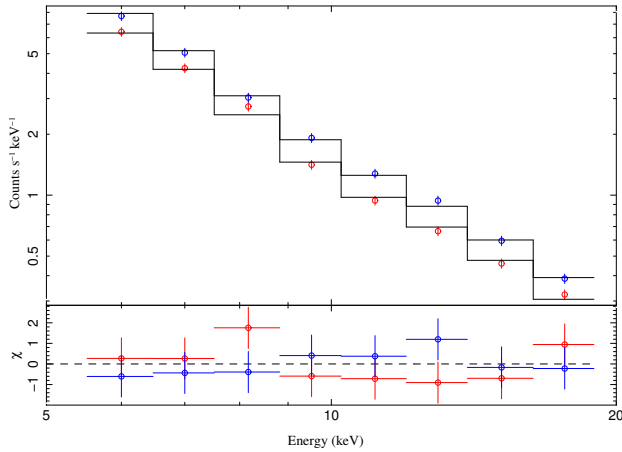


Figure 5.9: Both JEM-X instruments fitted with the broken power law model. The first JEM-X instrument is red and the second is blue in this plot. The different trends can be seen in this plot

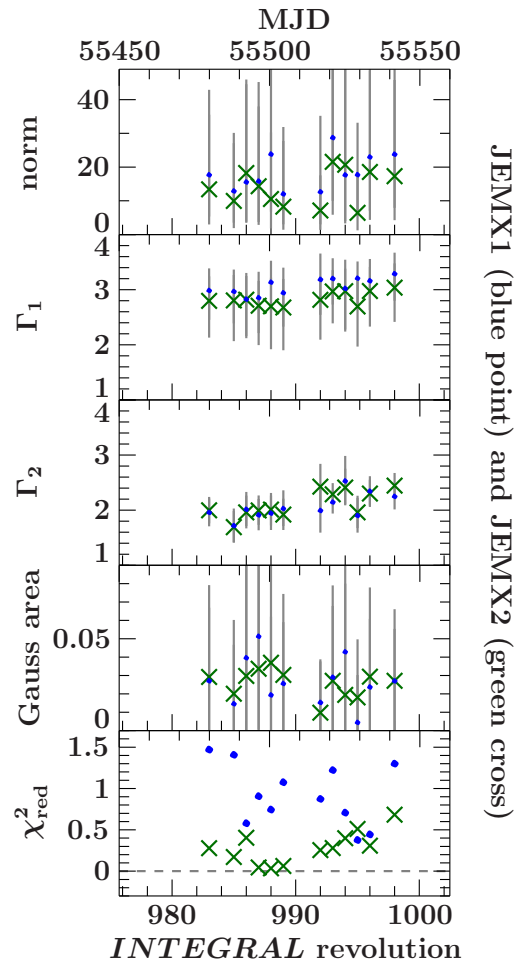


Figure 5.10: Parameters of the broken power law model with the Fe $K\alpha$ line. Parameter of the revolution 0938 of both instruments: JEM-X 1 Rev0938: $\chi_{red}^2 = 1.47$, Norm = 18_{-12}^{+25} , $\Gamma_1 = 3.0_{-0.5}^{+0.4}$, $\Gamma_2 = 2.0_{-0.2}^{+0.3}$, Area_{Gauss} = $0.03_{-0.03}^{+0.04}$. JEM-X 2 Rev0938: $\chi_{red}^2 = 0.28$, Norm = 13_{-10}^{+22} , $\Gamma_1 = 2.8_{-0.7}^{+0.4}$, $\Gamma_2 = 2.0 \pm 0.2$, Area_{Gauss} = $0.03_{-0.03}^{+0.05}$

are in a small range over the two flavors and also the area of the Gauss curve of the Fe $K\alpha$ have nearly the same value. And finally the χ_{red}^2 has good values especially of the second JEM-X module. The difference between both JEM-X instruments is the different trend for the slopes as shown for an example revolution on Fig. 5.9.

The last model, the `compTT` fit function, has really bad residuals and the χ_{red}^2 values are mostly between 3 and 7. This model also does not fit the data well, it needs an additional reflective component (Wilms et al., 2006, uses this additional component in the RXTE fittings) but this is not used in this work due to the poor quality of the data. So the `bknpower` model is suited well for fitting the JEM-X data and has to be tried to fit the overall data from ISGRI and JEM-X together.

5.5 Combined Spectra of ISGRI and JEMX

In this final section of the analysis part of this work, all data from the instruments of the *INTEGRAL* reduced in the previous Chapters are brought together. The overall spectra of

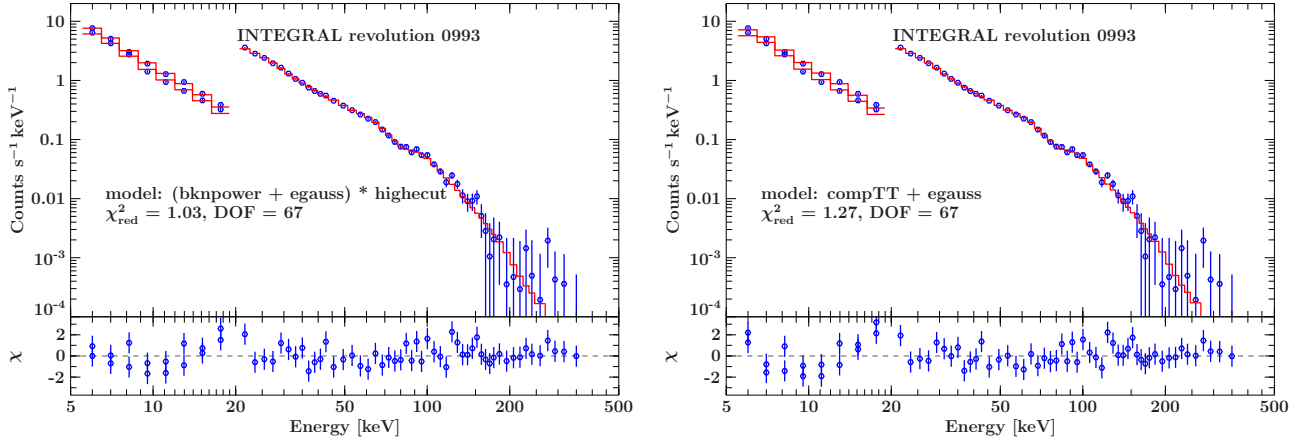


Figure 5.11: The overall spectrum of the revolution 0993 fitted with the broken power law model with a Fe $K\alpha$ line and an additional high energy cutoff (left) and fitted with the Comptonization model also with a Fe $K\alpha$ line (right). Parameter of the fittings: Left: $\chi_{\text{red}}^2 = 1.03$, $\text{Norm} = 19_{-11}^{+20}$, $\Gamma_1 = 2.8_{-0.4}^{+0.3}$, $\Gamma_2 = 2.54 \pm 0.08$, $\text{Area}_{\text{Gauss}} = 0.04 \pm 0.04$, $E_{\text{cut}} = 20_{-0}^{+4}$, $E_{\text{fold}} = 140_{-30}^{+50}$; Right: $\chi_{\text{red}}^2 = 1.27$, $\text{Norm} = 0.016_{-0.005}^{+0.006}$, $T_0 [\text{keV}] = 1.0$, $kT [\text{keV}] = 90_{-30}^{+50}$, $\tau_p = 0.08_{-0.06}^{+0.10}$, $\text{Compton-}y = 0.06$, $\text{Area}_{\text{Gauss}} = 0.077 \pm 0.017$

each revolution were fitted with the two best fitting models, once the `bknpower` model with additional an `egauss` function simulating the Fe $K\alpha$ line and with or without a `highecut` function and once the `compTT` model with also an `egauss` function.

All the parameters of this fits are attached in the Appendix A table A.16, A.17 and A.18.

The three data sets of each revolution were loaded in the ISIS tool and once again there fitted by the chosen models by a written script. The statistic error were the same for each Instrument as before and to fit the data correctly there were additional constant factors in the fit models. These constants take into account the different normalizations of the instruments. The combination of broken power law and the Fe $k\alpha$ line fit well with the data. But with additional a high energy cutoff function the residuals and the χ_{red}^2 become better. The parameter of the cutoff function E_c is set to minimum of 20 keV so it do not merge with the E_{break} of 10 keV of the `bknpower` model. The E_{fold} values are mostly below 500 keV, i.e. even in the soft state an exponential cutoff is detected in the combined data.

The `compTT` model fit also well with the data and the χ_{red}^2 can be compared with the other model. Although this model do not fit well with the JEM-X data, so the χ_{red}^2 value get better because of the good fit of the ISGRI data with this model and the additional Fe $K\alpha$ line.

The Fig. 5.11 shows as example the revolution 0993 with the two best fitting models. The residuals of both plots have the same shape but the χ_{red}^2 vales are significantly different as expected due to the bad fit of the `compTT` model of the JEM-X data. The Fig. 5.12 and 5.13 shows the parameter of this two model combinations.

The different flavors of the revolutions can also be recognize in this parameters. The Γ values of the broken power law model are slightly in different ranges in the two flavors. The first flavor has values between 2.5 and 2.7 for Γ_1 and between 2.3 and 2.5 for Γ_2 but the second flavor has vales between 2.8 and 3.1 for Γ_1 and between 2.4 and 2.8 for Γ_2 . As well as the τ_p and the kT values (120 to 310 keV for the first flavor and 90 to 200 keV for the second) change a bit with the flavors. The values of τ_p are around 0.01 with one exclusion of 0.09 in the first flavor and the values in the second are between 0.01 and 0.10.

An overview of the whole residuals and χ_{red}^2 is given in Fig. 5.14. Mostly all residuals have peaks in the same energies that can be caused by the standard ARF. The χ_{red}^2 of both models are in the same range and the broken power law model fits slightly better. Wilms et al. (2006) also saw this behavior.

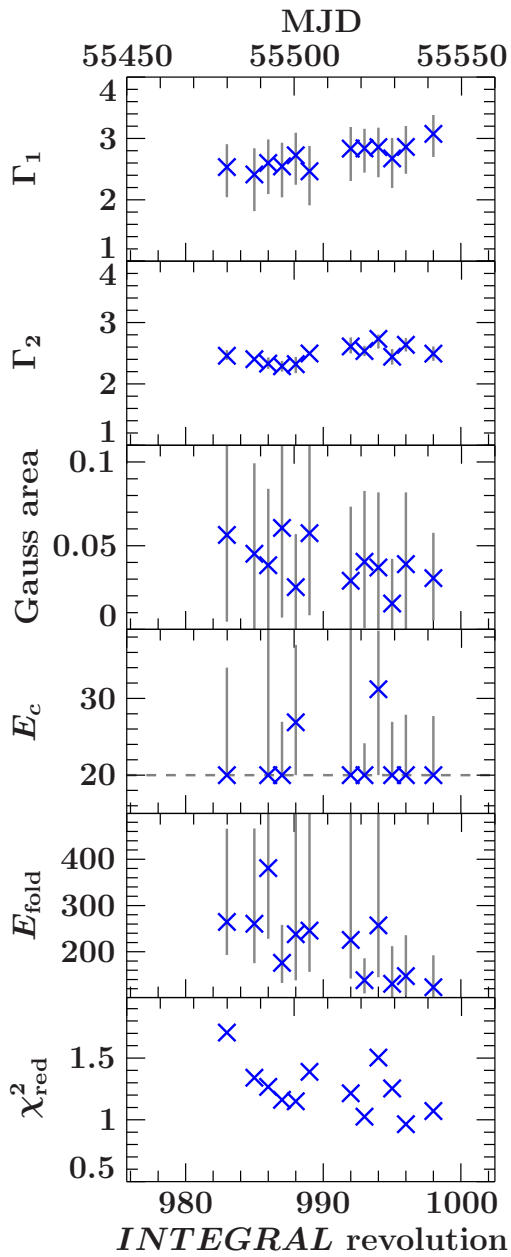


Figure 5.12: *Fit Parameter of the broken power law model with a Fe $K\alpha$ line and an exponential cutoff of the combined spectra*

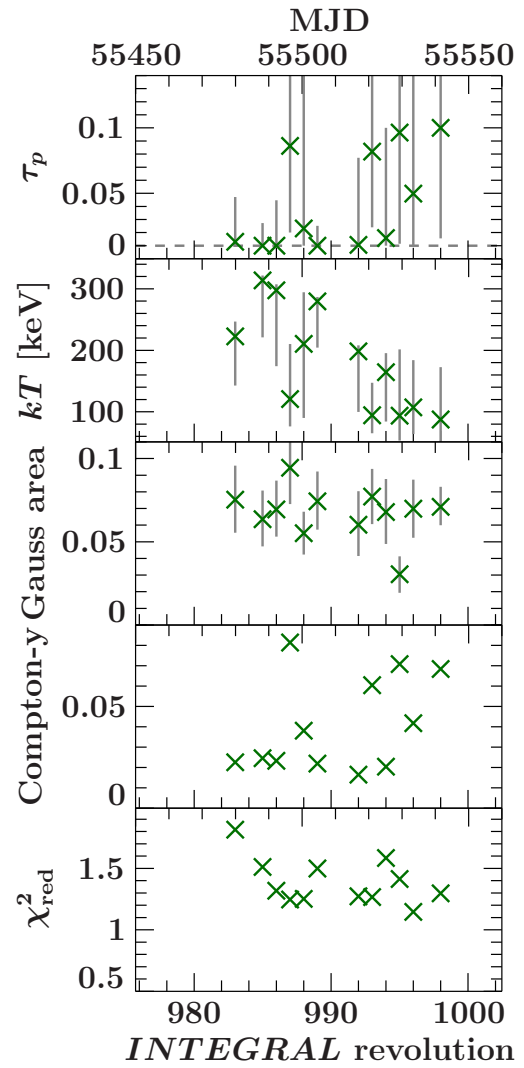


Figure 5.13: *Fit Parameter of the compTT model with a Fe $K\alpha$ line of the combined spectra*

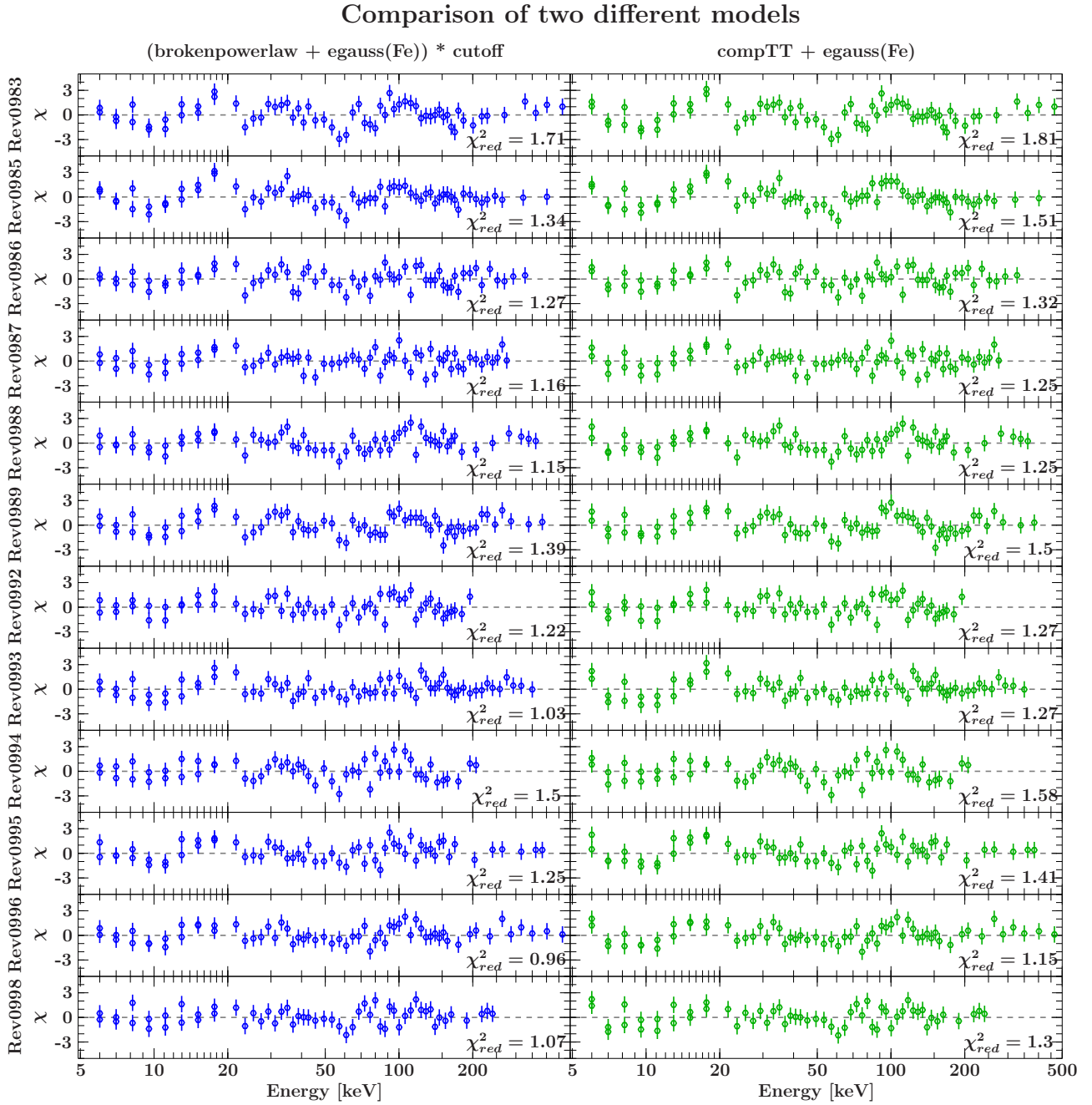


Figure 5.14: All residuals of the different revolutions fitted with the broken power law model and the Comptonization model.

Chapter 6

Summary and Discussion

6.1 ISGRI

To summarize the results of this analysis the problems have to be referred to again shortly. The first thing was the choice of the models to fit the available data. The data of this high energy spectra are best described with simple models. And it was seen that all residuals of these fits have the same shape and mostly the same peaks, so there has to be another systematic factor that biases the data. With a beta version of a new ARF the shape and the peaks became slightly better. But some problems like the first bin around 20 keV did not improve much and so the new ARF was not used for the analysis yet. Due to the calibration problems it was not able to search for a high energy excess (hard tail).

6.2 Overall Data

After adding the JEM-X data to the analysis, new models were chosen to fit the whole spectrum. And the analysis could be brought to a satisfactory result. The combination of the broken power law model, a Gaussian model to simulate the Fe $K\alpha$ line and a high energy exponential cutoff gives the best results.

But the analytical Comptonization model by Titarchuk (1994) in combination with also the Fe $K\alpha$ line is close to that results and has a better physical background. Wilms et al. (2006) analyzed the parameter of the fits and their correlations to each other. For the broken power law model the soft power law index Γ_1 and the hard power law index Γ_2 were shown to be correlated. The Fig. 6.1 shows the data from the paper (red diamonds) and the parameters from this work (blue diamonds). The data do not match well but the area is close to the area of the soft state parameters of the paper. In Fig. 6.2 Γ_1 are plotted against the E_{fold} parameter and shows the same result. Here it has to be mentioned that this work and the paper used different instruments and especially the JEM-X data has a bad quality. There were also some problems with the used instruments, such as the structure in the residuals. And also it has to be taken into account that the ISGRI and the two JEM-X instruments have different behaviors which causes problems.

Also there were correlation plots between some calculated parameters of the Comptonization model. In the Fig. 6.1 the electron temperature of the Comptonization plasma and optical depth are plotted against each other and also the red data points were from the paper and the blue from this work. The data from this work almost exclusively is above the data from the paper.

Wilms et al. (2006) also calculated the Compton- y value¹ for the data. The values of the soft state are mostly between 0.01 and 0.10 with some single values from 0.10 to 0.50 for the y

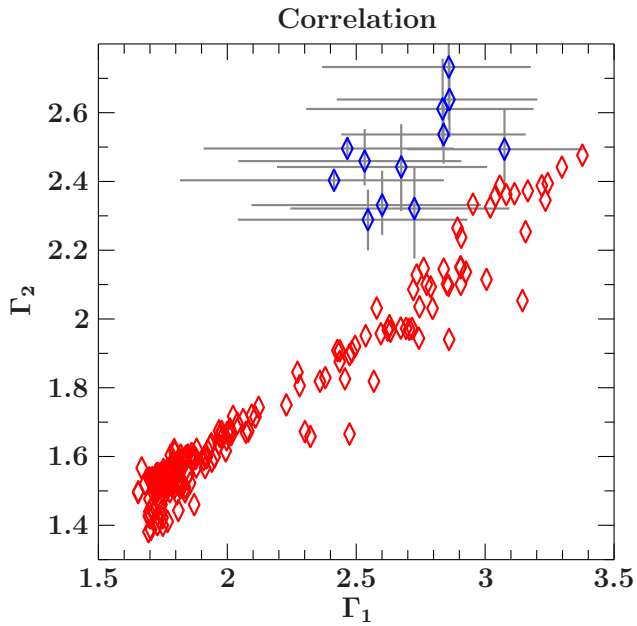


Figure 6.1: Correlation between the two parameters Γ_1 and Γ_2 of the broken power law model. The red data points are from Fig. 3 from Wilms et al. (2006) and the blue one are from this work.

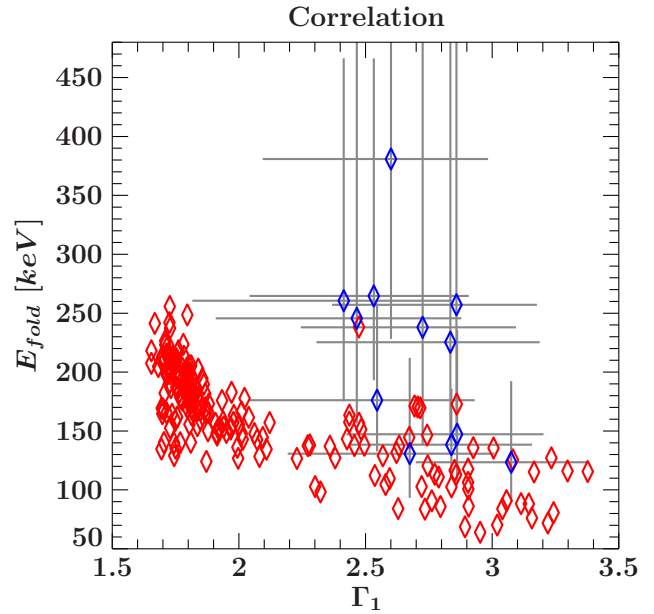


Figure 6.2: Correlation between two parameters Γ_1 and E_{fold} of the broken power law model. The red data points are from Fig.4 from Wilms et al. (2006) and the blue one are from this work.

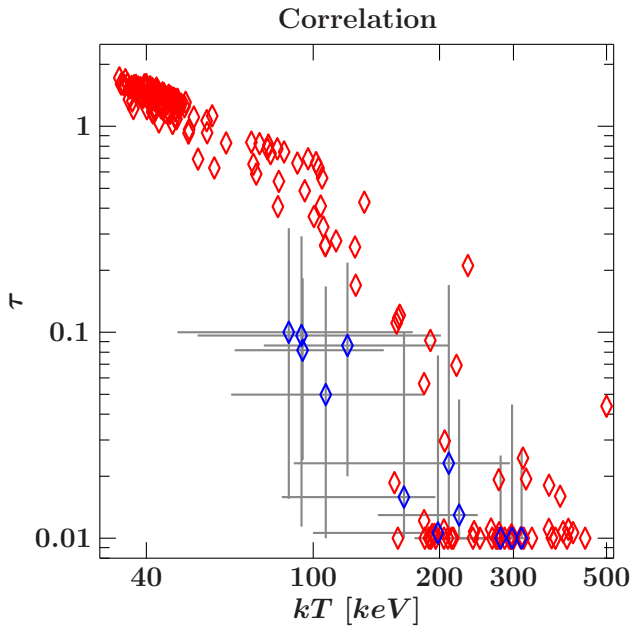


Figure 6.3: Correlation between the two parameters the electron temperature of the Comptonization plasma and optical depth τ of the Comptonization model. The red data points are from Fig. 5 from Wilms et al. (2006) and the blue one are from this work.

parameter. This calculation done with the data of this work results in values between 0.02 and 0.08 for the soft state. So this values are comparable with the values found in the paper, although the energy range in Wilms et al. (2006) is from 3 to 200 keV and were extracted from other astronomical devices.

So in conclusion the *INTEGRAL* data can be compared to the other data and with a new OSA version including a new and better ARF the small differences might be solved.

¹The formula of the Compton-y parameter given in Wilms et al. (2006) is $y = \frac{4kT}{m_e c^2} \max(\tau_p, \tau_p^2)$. It is defined as $y = (\text{Number of scatterings}) * (\text{Energy gain per scattering})$.

Appendix A

Appendix

Table A.1: Best fit parameters of the power law model for the ISGRI data

Revolution	DOF	χ^2	χ^2_{red}	Norm [keV ⁻¹ s ⁻¹ cm ⁻²]	Γ	Flux in 20-200 keV [keV s ⁻¹ cm ⁻²]
rev0929	55	725.89	13.70	$5.36^{+0.20}_{-0.19}$	1.945 ± 0.009	15.52
rev0938	56	450.29	8.34	5.9 ± 0.2	2.050 ± 0.010	11.07
rev0983	49	73.95	1.57	$18.2^{+1.4}_{-1.3}$	2.653 ± 0.020	3.05
rev0985	49	56.07	1.19	8.4 ± 0.6	2.432 ± 0.019	3.37
rev0986	49	61.44	1.31	$8.5^{+0.8}_{-0.7}$	2.46 ± 0.03	2.99
rev0987	49	63.46	1.35	$15.6^{+1.5}_{-1.4}$	$2.56^{+0.03}_{-0.02}$	3.71
rev0988	46	49.29	1.12	$6.8^{+1.1}_{-0.9}$	2.51 ± 0.04	2.01
rev0989	50	66.85	1.39	$10.1^{+0.8}_{-0.7}$	2.52 ± 0.02	2.84
rev0992	41	49.49	1.27	18 ± 2	2.81 ± 0.03	1.66
rev0993	51	46.75	0.95	27 ± 2	2.87 ± 0.02	1.95
rev0994	39	65.53	1.77	20^{+3}_{-2}	2.87 ± 0.03	1.45
rev0995	44	42.63	1.01	$12.3^{+1.7}_{-1.4}$	2.78 ± 0.04	1.28
rev0996	47	40.84	0.91	27 ± 3	2.93 ± 0.03	1.57
rev0998	41	43.17	1.11	14 ± 2	2.83 ± 0.04	1.22

Table A.2: Best fit parameters of the cutoff power law model for the ISGRI data

Revolution	DOF	χ^2	χ^2_{red}	Norm [keV ⁻¹ s ⁻¹ cm ⁻²]	Γ	E_{fold} [keV]	Flux in 20-200 keV [keV s ⁻¹ cm ⁻²]
rev0929	55	99.22	1.91	$1.42^{+0.15}_{-0.14}$	1.52 ± 0.03	$(1.76^{+0.14}_{-0.13}) \times 10^2$	15.53
rev0938	56	93.74	1.77	1.9 ± 0.2	1.68 ± 0.04	$(1.9 \pm 0.2) \times 10^2$	10.96
rev0983	49	66.11	1.44	13^{+2}_{-3}	$2.54^{+0.04}_{-0.07}$	$(0.43^{+0.07}_{-0.16}) \times 10^3$	3.02
rev0985	49	52.85	1.15	$6.2^{+0.5}_{-0.8}$	$2.33^{+0.02}_{-0.04}$	$(0.50^{+0.00}_{-0.14}) \times 10^3$	3.33
rev0986	49	59.55	1.29	$6.5^{+0.6}_{-1.2}$	$2.37^{+0.03}_{-0.07}$	$(0.5^{+0.0}_{-0.2}) \times 10^3$	2.95
rev0987	49	49.14	1.07	9^{+3}_{-2}	$2.36^{+0.09}_{-0.10}$	$(2.4^{+1.9}_{-0.7}) \times 10^2$	3.61
rev0988	46	48.72	1.13	$5.3^{+0.8}_{-1.6}$	$2.42^{+0.04}_{-0.13}$	$(0.5^{+0.0}_{-0.3}) \times 10^3$	1.98
rev0989	50	64.05	1.36	$7.6^{+0.6}_{-1.1}$	$2.42^{+0.02}_{-0.05}$	$(0.50^{+0.00}_{-0.17}) \times 10^3$	2.81
rev0992	41	45.32	1.19	12 ± 3	$2.67^{+0.08}_{-0.12}$	$(0.32^{+0.18}_{-0.15}) \times 10^3$	1.62
rev0993	51	33.09	0.69	15^{+5}_{-4}	$2.67^{+0.09}_{-0.10}$	$(2.3^{+1.9}_{-0.7}) \times 10^2$	1.91
rev0994	39	60.88	1.69	13^{+5}_{-4}	$2.71^{+0.11}_{-0.14}$	$(0.3^{+0.2}_{-0.1}) \times 10^3$	1.42
rev0995	44	39.01	0.95	8 ± 3	$2.63^{+0.09}_{-0.14}$	$(0.3^{+0.2}_{-0.1}) \times 10^3$	1.26
rev0996	47	36.26	0.82	18^{+6}_{-5}	$2.78^{+0.09}_{-0.13}$	$(0.3^{+0.2}_{-0.1}) \times 10^3$	1.54
rev0998	41	37.60	0.99	8^{+4}_{-3}	$2.62^{+0.15}_{-0.16}$	$(0.2^{+0.3}_{-0.1}) \times 10^3$	1.18

Table A.3: Best fit parameters of the compTT model for the ISGRI data

Revolution	DOF	χ^2	χ^2_{red}	Norm	T_0 [keV]	kT [keV]	τ_p	Compton-y	Flux in 20-200keV [keV s ⁻¹ cm ⁻²]
rev0929	55	77.92	1.50	0.034 ± 0.002	1.0	55^{+4}_{-3}	$1.04^{+0.08}_{-0.09}$	0.47	15.55
rev0938	56	88.03	1.66	$0.027^{+0.003}_{-0.005}$	1.0	61^{+13}_{-7}	$0.78^{+0.12}_{-0.18}$	0.37	10.95
rev0983	49	67.56	1.47	$(0.74^{+0.19}_{-0.04}) \times 10^{-2}$	1.0	$(2.4^{+0.1}_{-0.5}) \times 10^2$	$0.010^{+0.012}_{-0.000}$	0.02	3.00
rev0985	49	54.94	1.19	$(0.42^{+0.09}_{-0.02}) \times 10^{-2}$	1.0	$(3.1^{+0.1}_{-0.6}) \times 10^2$	$0.010^{+0.009}_{-0.000}$	0.02	3.31
rev0986	49	60.63	1.32	$(0.42^{+0.18}_{-0.03}) \times 10^{-2}$	1.0	$(3.0^{+0.1}_{-1.0}) \times 10^2$	$0.01^{+0.02}_{-0.00}$	0.02	2.94
rev0987	49	49.13	1.07	$0.010^{+0.006}_{-0.003}$	1.0	$(1.8^{+0.9}_{-0.7}) \times 10^2$	$0.03^{+0.09}_{-0.02}$	0.04	3.61
rev0988	46	49.24	1.15	$(0.3^{+0.3}_{-0.0}) \times 10^{-2}$	1.0	$(2.8^{+0.1}_{-1.4}) \times 10^2$	$0.01^{+0.06}_{-0.00}$	0.02	1.97
rev0989	50	66.59	1.42	$(0.47^{+0.11}_{-0.03}) \times 10^{-2}$	1.0	$(2.8^{+0.1}_{-0.6}) \times 10^2$	$0.010^{+0.010}_{-0.000}$	0.02	2.79
rev0992	41	45.58	1.20	$0.007^{+0.004}_{-0.001}$	1.0	$(2.0^{+0.1}_{-0.8}) \times 10^2$	$0.01^{+0.04}_{-0.00}$	0.02	1.62
rev0993	51	33.10	0.69	$0.010^{+0.006}_{-0.001}$	1.0	$(1.8^{+0.2}_{-0.7}) \times 10^2$	$0.01^{+0.05}_{-0.00}$	0.02	1.91
rev0994	39	60.93	1.69	$0.007^{+0.006}_{-0.001}$	1.0	$(1.9^{+0.1}_{-0.9}) \times 10^2$	$0.01^{+0.07}_{-0.00}$	0.01	1.42
rev0995	44	39.08	0.95	$(0.5^{+0.4}_{-0.0}) \times 10^{-2}$	1.0	$(2.1^{+0.1}_{-1.1}) \times 10^2$	$0.01^{+0.07}_{-0.00}$	0.02	1.25
rev0996	47	36.51	0.83	$0.009^{+0.005}_{-0.001}$	1.0	$(1.8^{+0.1}_{-0.7}) \times 10^2$	$0.01^{+0.04}_{-0.00}$	0.01	1.53
rev0998	41	37.60	0.99	$0.007^{+0.007}_{-0.002}$	1.0	$(1.5^{+0.5}_{-0.8}) \times 10^2$	$0.02^{+0.15}_{-0.01}$	0.03	1.18

Table A.4: Best fit parameters of the power law model for the ISGRI data with the new ARF

Revolution	DOF	χ^2	χ^2_{red}	Norm [keV ⁻¹ s ⁻¹ cm ⁻²]	Γ	Flux in 20-200 keV [keV s ⁻¹ cm ⁻²]
rev0929	55	717.76	13.54	5.21 ^{+0.19} _{-0.18}	1.932 ± 0.009	15.88
rev0938	56	521.82	9.66	5.8 ± 0.2	2.040 ± 0.010	11.32
rev0983	49	103.25	2.20	15.9 ^{+1.2} _{-1.1}	2.612 ± 0.019	3.14
rev0985	49	73.83	1.57	7.6 ± 0.5	2.398 ± 0.018	3.47
rev0986	49	73.17	1.56	7.4 ^{+0.7} _{-0.6}	2.42 ± 0.02	3.09
rev0987	49	100.74	2.14	13.4 ^{+1.2} _{-1.1}	2.52 ± 0.02	3.83
rev0988	46	61.65	1.40	5.6 ^{+0.8} _{-0.7}	2.45 ± 0.04	2.09
rev0989	50	78.01	1.63	8.9 ^{+0.7} _{-0.6}	2.482 ± 0.020	2.93
rev0992	41	72.31	1.85	14.3 ^{+1.6} _{-1.4}	2.74 ± 0.03	1.71
rev0993	51	87.06	1.78	22.1 ^{+1.9} _{-1.8}	2.81 ± 0.02	2.01
rev0994	39	75.95	2.05	15.7 ^{+1.9} _{-1.7}	2.80 ± 0.03	1.50
rev0995	44	58.94	1.40	9.9 ^{+1.3} _{-1.1}	2.71 ± 0.03	1.33
rev0996	47	61.58	1.37	21 ± 2	2.86 ± 0.03	1.62
rev0998	41	60.49	1.55	11.2 ^{+1.6} _{-1.4}	2.76 ± 0.04	1.26

Table A.5: Best fit parameters of the cutoff power law model for the ISGRI data with the new ARF

Revolution	DOF	χ^2	χ^2_{red}	Norm [keV $^{-1}$ s $^{-1}$ cm $^{-2}$]	Γ	E_{fold} [keV]	Flux in 20-200 keV [keV s $^{-1}$ cm $^{-2}$]
rev0929	55	24.98	0.48	$1.21^{+0.14}_{-0.12}$	1.46 ± 0.03	$(1.53^{+0.12}_{-0.10}) \times 10^2$	15.88
rev0938	56	42.08	0.79	$1.45^{+0.18}_{-0.17}$	1.58 ± 0.04	$(1.47^{+0.13}_{-0.11}) \times 10^2$	11.19
rev0983	49	53.95	1.17	$7.0^{+1.6}_{-1.4}$	$2.32^{+0.07}_{-0.08}$	$(1.7^{+0.6}_{-0.3}) \times 10^2$	3.05
rev0985	49	39.03	0.85	$4.0^{+0.9}_{-0.7}$	2.17 ± 0.07	$(2.3^{+0.9}_{-0.5}) \times 10^2$	3.38
rev0986	49	52.08	1.13	$3.8^{+1.1}_{-0.9}$	2.18 ± 0.09	$(2.0^{+1.2}_{-0.6}) \times 10^2$	2.99
rev0987	49	50.19	1.09	$4.7^{+1.4}_{-1.1}$	$2.14^{+0.09}_{-0.10}$	$(1.3^{+0.4}_{-0.3}) \times 10^2$	3.65
rev0988	46	53.15	1.24	$2.9^{+1.4}_{-1.0}$	$2.21^{+0.14}_{-0.15}$	$(2^{+3}_{-1}) \times 10^2$	2.01
rev0989	50	46.59	0.99	$4.6^{+1.1}_{-0.9}$	$2.24^{+0.07}_{-0.08}$	$(2.1^{+0.9}_{-0.5}) \times 10^2$	2.85
rev0992	41	48.89	1.29	6 ± 2	2.42 ± 0.12	$(1.4^{+0.8}_{-0.4}) \times 10^2$	1.64
rev0993	51	34.56	0.72	8 ± 2	2.43 ± 0.10	$(1.2^{+0.4}_{-0.2}) \times 10^2$	1.93
rev0994	39	54.32	1.51	6^{+3}_{-2}	$2.46^{+0.13}_{-0.14}$	$(1.2^{+0.7}_{-0.4}) \times 10^2$	1.43
rev0995	44	39.68	0.97	$4.1^{+1.8}_{-1.3}$	$2.38^{+0.13}_{-0.14}$	$(1.3^{+0.8}_{-0.4}) \times 10^2$	1.27
rev0996	47	37.58	0.85	9 ± 3	$2.52^{+0.12}_{-0.13}$	$(1.3^{+0.7}_{-0.3}) \times 10^2$	1.55
rev0998	41	39.01	1.03	$3.9^{+2.0}_{-1.4}$	$2.36^{+0.15}_{-0.16}$	$(1.0^{+0.6}_{-0.3}) \times 10^2$	1.19

Table A.6: Best fit parameters of the *compTT* model for the ISGRI data with the new ARF

Revolution	DOF	χ^2	χ^2_{red}	Norm	T_0 [keV]	kT [keV]	τ_p	Compton-y	Flux in 20-200 keV [keV s ⁻¹ cm ⁻²]
rev0929	55	42.46	0.82	0.036 ± 0.002	1.0	53 ⁺⁴ ₋₃	1.08 ^{+0.08} _{-0.09}	0.48	15.91
rev0938	56	48.18	0.91	0.031 ± 0.003	1.0	53 ⁺⁷ ₋₄	0.91 ^{+0.10} _{-0.13}	0.38	11.20
rev0983	49	54.05	1.18	0.014 ^{+0.004} _{-0.005}	1.0	(1.1 ^{+0.6} _{-0.3}) × 10 ²	0.10 ^{+0.09} _{-0.07}	0.08	3.05
rev0985	49	39.04	0.85	0.007 ^{+0.003} _{-0.002}	1.0	(1.6 ^{+0.9} _{-0.5}) × 10 ²	0.07 ^{+0.09} _{-0.05}	0.08	3.38
rev0986	49	52.10	1.13	0.008 ^{+0.005} _{-0.003}	1.0	(1.4 ^{+1.2} _{-0.6}) × 10 ²	0.09 ^{+0.16} _{-0.07}	0.10	2.99
rev0987	49	50.22	1.09	0.022 ^{+0.009} _{-0.007}	1.0	(0.7 ^{+0.4} _{-0.2}) × 10 ²	0.3 ^{+0.3} _{-0.2}	0.15	3.65
rev0988	46	53.18	1.24	0.007 ^{+0.006} _{-0.004}	1.0	(1.2 ^{+1.8} _{-0.7}) × 10 ²	0.1 ^{+0.3} _{-0.1}	0.09	2.01
rev0989	50	46.61	0.99	0.008 ± 0.003	1.0	(1.5 ^{+0.9} _{-0.5}) × 10 ²	0.06 ^{+0.09} _{-0.05}	0.07	2.85
rev0992	41	48.94	1.29	0.013 ^{+0.007} _{-0.005}	1.0	(0.9 ^{+0.7} _{-0.3}) × 10 ²	0.12 ^{+0.20} _{-0.10}	0.08	1.64
rev0993	51	34.68	0.72	0.020 ^{+0.007} _{-0.006}	1.0	(0.7 ^{+0.4} _{-0.2}) × 10 ²	0.17 ^{+0.16} _{-0.10}	0.09	1.93
rev0994	39	54.37	1.51	0.014 ^{+0.008} _{-0.006}	1.0	76 ⁺¹⁴ ₋₃₁	0.1 ^{+0.2} _{-0.1}	0.08	1.43
rev0995	44	39.74	0.97	0.010 ^{+0.006} _{-0.005}	1.0	(0.8 ^{+0.8} _{-0.3}) × 10 ²	0.2 ^{+0.3} _{-0.1}	0.09	1.27
rev0996	47	37.65	0.86	0.016 ^{+0.008} _{-0.007}	1.0	79 ⁺¹⁵ ₋₃₁	0.11 ^{+0.19} _{-0.09}	0.07	1.55
rev0998	41	39.13	1.03	0.014 ^{+0.007} _{-0.006}	1.0	(0.6 ^{+0.6} _{-0.2}) × 10 ²	0.3 ^{+0.3} _{-0.2}	0.11	1.19

Table A.7: Best fit parameters of the power law model for the ISGRI data with maximum 10 degree angular distant

Revolution	DOF	χ^2	χ^2_{red}	Norm [keV ⁻¹ s ⁻¹ cm ⁻²]	Γ	Flux in 20-200 keV [keV s ⁻¹ cm ⁻²]
rev0929	55	725.87	13.70	5.36 ^{+0.20} _{-0.19}	1.945 ± 0.009	15.52
rev0938	56	450.29	8.34	5.9 ± 0.2	2.050 ± 0.010	11.07
rev0983	51	74.51	1.52	17.8 ^{+1.4} _{-1.3}	2.65 ± 0.02	3.03
rev0985	49	54.19	1.15	8.3 ± 0.6	2.425 ± 0.020	3.40
rev0986	46	54.72	1.24	8.6 ^{+0.9} _{-0.8}	2.46 ± 0.03	3.08
rev0987	46	49.96	1.14	15.9 ^{+1.5} _{-1.4}	2.55 ± 0.03	3.95
rev0988	46	49.30	1.12	6.8 ^{+1.1} _{-0.9}	2.51 ± 0.04	2.01
rev0989	50	65.56	1.37	10.2 ± 0.8	2.52 ± 0.02	2.86
rev0992	42	53.04	1.33	18 ± 2	2.81 ± 0.03	1.68
rev0993	49	45.40	0.97	27 ± 2	2.87 ± 0.02	1.95
rev0994	38	61.86	1.72	19 ⁺³ ₋₂	2.86 ± 0.04	1.46
rev0995	45	40.26	0.94	11.4 ^{+1.6} _{-1.4}	2.76 ± 0.04	1.26
rev0996	47	33.80	0.75	27 ± 3	2.93 ± 0.03	1.57
rev0998	41	43.16	1.11	14 ± 2	2.83 ± 0.04	1.22

Table A.8: Best fit parameters of the cutoff power law model for the ISGRI data with maximum 10 degree angular distant

Revolution	DOF	χ^2	χ^2_{red}	Norm [keV ⁻¹ s ⁻¹ cm ⁻²]	Γ	E_{fold} [keV]	Flux in 20-200 keV [keV s ⁻¹ cm ⁻²]
rev0929	55	99.25	1.91	$1.42^{+0.15}_{-0.14}$	1.52 ± 0.03	$(1.76^{+0.14}_{-0.13}) \times 10^2$	15.53
rev0938	56	93.74	1.77	1.9 ± 0.2	1.68 ± 0.04	$(1.9 \pm 0.2) \times 10^2$	10.96
rev0983	51	68.29	1.42	13^{+1}_{-3}	$2.54^{+0.03}_{-0.08}$	$(0.46^{+0.04}_{-0.19}) \times 10^3$	2.99
rev0985	49	52.01	1.13	$6.2^{+0.5}_{-0.7}$	$2.32^{+0.02}_{-0.04}$	$(0.50^{+0.00}_{-0.14}) \times 10^3$	3.36
rev0986	46	54.47	1.27	$6.5^{+0.7}_{-1.1}$	$2.36^{+0.03}_{-0.06}$	$(0.50^{+0.00}_{-0.19}) \times 10^3$	3.03
rev0987	46	36.99	0.86	9^{+3}_{-2}	2.36 ± 0.10	$(2^{+2}_{-1}) \times 10^2$	3.85
rev0988	46	48.72	1.13	$5.3^{+0.8}_{-1.6}$	$2.42^{+0.04}_{-0.13}$	$(0.5^{+0.0}_{-0.3}) \times 10^3$	1.98
rev0989	50	61.31	1.30	$7.7^{+0.6}_{-1.3}$	$2.42^{+0.02}_{-0.07}$	$(0.50^{+0.00}_{-0.19}) \times 10^3$	2.82
rev0992	42	47.65	1.22	12^{+4}_{-3}	$2.65^{+0.10}_{-0.12}$	$(0.3^{+0.2}_{-0.1}) \times 10^3$	1.64
rev0993	49	31.95	0.69	15^{+5}_{-4}	2.67 ± 0.10	$(2.3^{+1.9}_{-0.7}) \times 10^2$	1.90
rev0994	38	58.29	1.67	13 ± 4	$2.71^{+0.10}_{-0.14}$	$(0.3^{+0.2}_{-0.1}) \times 10^3$	1.43
rev0995	45	37.86	0.90	8^{+2}_{-3}	$2.64^{+0.07}_{-0.14}$	$(0.35^{+0.15}_{-0.18}) \times 10^3$	1.24
rev0996	47	29.72	0.68	18 ± 5	$2.78^{+0.09}_{-0.13}$	$(0.3^{+0.2}_{-0.1}) \times 10^3$	1.54
rev0998	41	37.59	0.99	8^{+4}_{-3}	$2.62^{+0.15}_{-0.16}$	$(0.2^{+0.3}_{-0.1}) \times 10^3$	1.18

Table A.9: Best fit parameters of the *compTT* model for the ISGRI data with maximum 10 degree angular distant

Revolution	DOF	χ^2	χ^2_{red}	Norm	T_0 [keV]	kT [keV]	τ_p	Compton-y	Flux in 20-200keV [keV s ⁻¹ cm ⁻²]
rev0929	55	77.94	1.50	0.034 ± 0.002	1.0	55^{+4}_{-3}	$1.04^{+0.08}_{-0.09}$	0.47	15.55
rev0938	56	88.02	1.66	$0.027^{+0.003}_{-0.005}$	1.0	61^{+13}_{-7}	$0.78^{+0.12}_{-0.18}$	0.37	10.95
rev0983	51	69.99	1.46	$(0.73^{+0.19}_{-0.04}) \times 10^{-2}$	1.0	$(2.4^{+0.1}_{-0.5}) \times 10^2$	$0.010^{+0.012}_{-0.000}$	0.02	2.97
rev0985	49	54.14	1.18	$(0.41^{+0.09}_{-0.02}) \times 10^{-2}$	1.0	$(3.1^{+0.1}_{-0.6}) \times 10^2$	$0.010^{+0.009}_{-0.000}$	0.02	3.35
rev0986	46	55.91	1.30	$(0.43^{+0.17}_{-0.03}) \times 10^{-2}$	1.0	$(3.0^{+0.1}_{-0.9}) \times 10^2$	$0.010^{+0.018}_{-0.000}$	0.02	3.02
rev0987	46	36.98	0.86	$0.010^{+0.006}_{-0.003}$	1.0	$(1.8^{+0.9}_{-0.8}) \times 10^2$	$0.03^{+0.09}_{-0.02}$	0.04	3.85
rev0988	46	49.25	1.15	$(0.3^{+0.3}_{-0.0}) \times 10^{-2}$	1.0	$(2.8^{+0.1}_{-1.4}) \times 10^2$	$0.01^{+0.06}_{-0.00}$	0.02	1.97
rev0989	50	62.97	1.34	$(0.47^{+0.13}_{-0.03}) \times 10^{-2}$	1.0	$(2.8^{+0.1}_{-0.7}) \times 10^2$	$0.010^{+0.013}_{-0.000}$	0.02	2.81
rev0992	42	47.69	1.22	$0.007^{+0.005}_{-0.001}$	1.0	$(2.0^{+0.1}_{-1.0}) \times 10^2$	$0.01^{+0.06}_{-0.00}$	0.02	1.64
rev0993	49	31.96	0.69	$0.010^{+0.006}_{-0.001}$	1.0	$(1.8^{+0.2}_{-0.7}) \times 10^2$	$0.01^{+0.05}_{-0.00}$	0.02	1.90
rev0994	38	58.42	1.67	$0.007^{+0.006}_{-0.001}$	1.0	$(1.9^{+0.1}_{-0.9}) \times 10^2$	$0.01^{+0.06}_{-0.00}$	0.01	1.42
rev0995	45	38.10	0.91	$(0.4^{+0.4}_{-0.0}) \times 10^{-2}$	1.0	$(2.1^{+0.1}_{-1.0}) \times 10^2$	$0.01^{+0.06}_{-0.00}$	0.02	1.23
rev0996	47	30.04	0.68	$0.009^{+0.005}_{-0.001}$	1.0	$(1.8^{+0.1}_{-0.7}) \times 10^2$	$0.01^{+0.04}_{-0.00}$	0.01	1.53
rev0998	41	37.61	0.99	$0.006^{+0.008}_{-0.001}$	1.0	$(1.6^{+0.4}_{-1.0}) \times 10^2$	$0.02^{+0.16}_{-0.01}$	0.02	1.18

Table A.10: Best fit parameters of the power law model for the ISGRI data of the summed spectra of the flavor ranges

Revolution	DOF	χ^2	χ_{red}^2	Norm [keV ⁻¹ s ⁻¹ cm ⁻²]	Γ	Flux in 20-200 keV [keV s ⁻¹ cm ⁻²]
rev098x	52	103.74	2.07	11.8 ^{+0.7} _{-0.6}	2.545 ± 0.014	3.03
rev099x	45	74.58	1.73	21.6 ^{+1.6} _{-1.5}	2.875 ± 0.019	1.55

Table A.11: Best fit parameters of the cutoff power law model for the ISGRI data of the summed spectra of the flavor ranges

Revolution	DOF	χ^2	χ_{red}^2	Norm [keV ⁻¹ s ⁻¹ cm ⁻²]	Γ	E_{fold} [keV]	Flux in 20-200 keV [keV s ⁻¹ cm ⁻²]
rev098x	52	84.94	1.73	8.1 ^{+0.9} _{-1.2}	2.42 ^{+0.03} _{-0.05}	(0.44 ^{+0.06} _{-0.12}) × 10 ³	3.00
rev099x	45	58.77	1.40	14 ± 3	2.71 ± 0.07	(0.3 ^{+0.2} _{-0.1}) × 10 ³	1.53

Table A.12: Best fit parameters of the compTT model for the ISGRI data of the summed spectra of the flavor ranges

Revolution	DOF	χ^2	χ_{red}^2	Norm	T_0 [keV]	kT [keV]	τ_p	Compton-y	Flux in 20-200 keV [keV s ⁻¹ cm ⁻²]
rev098x	52	86.45	1.76	(0.51 ^{+0.09} _{-0.02}) × 10 ⁻²	1.0	(2.8 ^{+0.0} _{-0.5}) × 10 ²	0.010 ^{+0.007} _{-0.000}	0.02	2.99
rev099x	45	59.54	1.42	(0.70 ^{+0.17} _{-0.03}) × 10 ⁻²	1.0	(1.9 ^{+0.0} _{-0.4}) × 10 ²	0.010 ^{+0.013} _{-0.000}	0.02	1.52

Table A.13: Best fit parameters of the broken power law model for the JEM-X data

Revolution	JEM-X	DOF	χ^2	χ^2_{red}	Norm [keV ⁻¹ s ⁻¹ cm ⁻²]	Γ_1	Γ_2	Flux in 20-200 keV [keV s ⁻¹ cm ⁻²]
rev0983	1	8	7.24	1.45	32^{+17}_{-11}	3.2 ± 0.2	$2.0^{+0.3}_{-0.2}$	4.53
rev0985	1	8	6.23	1.25	20^{+12}_{-8}	3.2 ± 0.2	1.7 ± 0.3	5.43
rev0986	1	8	3.80	0.76	32^{+20}_{-12}	3.1 ± 0.2	2.0 ± 0.3	5.17
rev0987	1	8	6.39	1.28	40^{+23}_{-15}	3.3 ± 0.2	1.9 ± 0.3	5.94
rev0988	1	8	3.59	0.72	36^{+22}_{-14}	3.3 ± 0.2	2.0 ± 0.3	4.39
rev0989	1	8	6.05	1.21	25^{+15}_{-10}	3.3 ± 0.2	2.0 ± 0.3	2.95
rev0992	1	8	4.76	0.95	24^{+17}_{-10}	3.5 ± 0.3	2.0 ± 0.4	1.86
rev0993	1	8	6.52	1.30	51^{+24}_{-17}	3.45 ± 0.19	2.2 ± 0.2	3.17
rev0994	1	8	5.10	1.02	45^{+32}_{-19}	3.4 ± 0.3	2.5 ± 0.4	1.51
rev0995	1	8	1.59	0.32	21^{+13}_{-8}	3.3 ± 0.2	1.9 ± 0.3	3.02
rev0996	1	8	3.00	0.60	40^{+21}_{-14}	3.4 ± 0.2	2.3 ± 0.3	1.97
rev0998	1	8	7.88	1.58	50^{+24}_{-17}	$3.61^{+0.19}_{-0.20}$	2.3 ± 0.2	1.78
rev0983	2	8	2.17	0.43	25^{+14}_{-9}	3.1 ± 0.2	2.0 ± 0.2	5.01
rev0985	2	8	1.47	0.29	18^{+11}_{-7}	3.1 ± 0.2	1.7 ± 0.3	6.54
rev0986	2	8	2.19	0.44	30^{+19}_{-12}	3.0 ± 0.2	2.0 ± 0.3	6.87
rev0987	2	8	0.97	0.19	26^{+15}_{-10}	3.0 ± 0.2	2.0 ± 0.3	6.57
rev0988	2	8	1.60	0.32	24^{+15}_{-9}	3.1 ± 0.2	2.0 ± 0.3	4.81
rev0989	2	8	1.76	0.35	19^{+11}_{-7}	3.0 ± 0.2	1.9 ± 0.3	4.73
rev0992	2	8	1.39	0.28	11^{+8}_{-5}	3.0 ± 0.3	2.4 ± 0.4	1.19
rev0993	2	8	1.95	0.39	36^{+18}_{-12}	3.19 ± 0.20	2.28 ± 0.20	3.23
rev0994	2	8	1.92	0.38	30^{+21}_{-13}	3.1 ± 0.3	2.4 ± 0.3	2.47
rev0995	2	8	3.06	0.61	12^{+8}_{-5}	3.0 ± 0.2	2.0 ± 0.3	3.24
rev0996	2	8	2.38	0.48	35^{+19}_{-13}	3.3 ± 0.2	2.3 ± 0.2	2.67
rev0998	2	8	4.25	0.85	35^{+18}_{-12}	3.3 ± 0.2	2.4 ± 0.2	1.70

Table A.14: Best fit parameters of the broken power law model with a Fe K α line for the JEM-X data

Revolution	JEM-X	DOF	χ^2	χ^2_{red}	Norm [keV $^{-1}$ s $^{-1}$ cm $^{-2}$]	Γ_1	Γ_2	Area _{Gauss} [photons s $^{-1}$ cm $^{-2}$]	Flux in 20-200 keV [keV s $^{-1}$ cm $^{-2}$]
rev0983	1	8	5.88	1.47	18 $^{+25}_{-12}$	3.0 $^{+0.4}_{-0.5}$	2.0 $^{+0.3}_{-0.2}$	0.03 $^{+0.04}_{-0.03}$	4.56
rev0985	1	8	5.63	1.41	13 $^{+17}_{-9}$	3.0 $^{+0.4}_{-0.6}$	1.7 \pm 0.3	0.01 $^{+0.03}_{-0.01}$	5.47
rev0986	1	8	2.32	0.58	16 $^{+29}_{-12}$	2.8 $^{+0.5}_{-0.7}$	2.0 \pm 0.3	0.04 $^{+0.06}_{-0.04}$	5.18
rev0987	1	8	3.62	0.91	16 $^{+29}_{-12}$	2.9 $^{+0.5}_{-0.6}$	1.9 \pm 0.3	0.05 \pm 0.05	5.99
rev0988	1	8	2.98	0.74	24 $^{+31}_{-17}$	3.1 $^{+0.4}_{-0.6}$	1.9 \pm 0.3	0.02 $^{+0.04}_{-0.02}$	4.44
rev0989	1	8	4.30	1.08	12 $^{+20}_{-9}$	2.9 $^{+0.5}_{-0.6}$	2.0 \pm 0.3	0.03 \pm 0.03	2.99
rev0992	1	8	3.49	0.87	13 $^{+23}_{-10}$	3.2 $^{+0.5}_{-0.6}$	2.0 \pm 0.4	0.02 \pm 0.02	1.92
rev0993	1	8	4.89	1.22	29 $^{+37}_{-19}$	3.2 $^{+0.4}_{-0.5}$	2.1 \pm 0.2	0.03 $^{+0.04}_{-0.03}$	3.19
rev0994	1	8	2.83	0.71	18 $^{+38}_{-14}$	3.0 $^{+0.5}_{-0.7}$	2.5 $^{+0.5}_{-0.4}$	0.04 $^{+0.05}_{-0.04}$	1.55
rev0995	1	8	1.51	0.38	18 $^{+15}_{-12}$	3.2 $^{+0.3}_{-0.5}$	1.9 \pm 0.3	\leq 0.03	3.04
rev0996	1	8	1.78	0.44	23 $^{+32}_{-16}$	3.2 $^{+0.4}_{-0.5}$	2.3 \pm 0.3	0.02 $^{+0.04}_{-0.02}$	1.98
rev0998	1	8	5.20	1.30	24 $^{+32}_{-16}$	3.3 $^{+0.4}_{-0.5}$	2.2 \pm 0.2	0.03 \pm 0.03	1.80
rev0983	2	8	1.11	0.28	13 $^{+22}_{-10}$	2.8 $^{+0.4}_{-0.7}$	2.0 \pm 0.2	0.03 $^{+0.05}_{-0.03}$	4.95
rev0985	2	8	0.68	0.17	10 $^{+17}_{-8}$	2.8 $^{+0.5}_{-0.7}$	1.7 \pm 0.3	0.02 $^{+0.04}_{-0.02}$	6.49
rev0986	2	8	1.62	0.40	18 $^{+28}_{-14}$	2.8 $^{+0.4}_{-0.7}$	2.0 \pm 0.3	0.03 $^{+0.07}_{-0.03}$	6.85
rev0987	2	8	0.18	0.04	14 $^{+24}_{-11}$	2.7 $^{+0.4}_{-0.7}$	2.0 \pm 0.3	0.03 $^{+0.07}_{-0.03}$	6.50
rev0988	2	8	0.14	0.03	11 $^{+20}_{-9}$	2.7 $^{+0.5}_{-0.8}$	2.0 \pm 0.3	0.04 $^{+0.05}_{-0.04}$	4.75
rev0989	2	8	0.25	0.06	8 $^{+19}_{-7}$	2.7 $^{+0.5}_{-0.8}$	1.9 \pm 0.3	0.03 $^{+0.04}_{-0.03}$	4.66
rev0992	2	8	1.02	0.25	7 $^{+10}_{-6}$	2.8 $^{+0.4}_{-0.7}$	2.4 \pm 0.4	0.01 $^{+0.03}_{-0.01}$	1.19
rev0993	2	8	1.12	0.28	22 $^{+28}_{-16}$	3.0 $^{+0.4}_{-0.6}$	2.3 \pm 0.2	0.03 $^{+0.05}_{-0.03}$	3.20
rev0994	2	8	1.59	0.40	21 $^{+29}_{-17}$	3.0 $^{+0.4}_{-0.7}$	2.4 \pm 0.3	0.02 $^{+0.06}_{-0.02}$	2.46
rev0995	2	8	2.05	0.51	6 $^{+12}_{-5}$	2.7 $^{+0.5}_{-0.7}$	2.0 \pm 0.3	0.02 $^{+0.03}_{-0.02}$	3.22
rev0996	2	8	1.23	0.31	19 $^{+30}_{-14}$	3.0 $^{+0.4}_{-0.6}$	2.3 \pm 0.2	0.03 $^{+0.05}_{-0.03}$	2.65
rev0998	2	8	2.73	0.68	17 $^{+28}_{-13}$	3.0 $^{+0.4}_{-0.6}$	2.4 \pm 0.2	0.03 $^{+0.04}_{-0.03}$	1.68

Table A.15: Best fit parameters of the compIT model for the JEM-X data

Revolution	JEM-X	DOF	χ^2	χ^2_{red}	Norm	T_0 [keV]	kT [keV]	τ_p	Compton-y	Flux in 20-200 keV [keV s ⁻¹ cm ⁻²]
rev0983	1	8	43.95	8.79	$0.01^{+0.12}_{-0.00}$	1.0	$(1.9^{+0.3}_{-1.8}) \times 10^2$	≤ 1.6	0.01	1.32
rev0985	1	8	36.83	7.37	≤ 19	1.0	$(2^{+0}_{-2}) \times 10^2$	≤ 2	0.02	1.24
rev0986	1	8	26.18	5.24	≤ 19	1.0	$(1.9^{+0.3}_{-1.8}) \times 10^2$	≤ 2	0.01	1.60
rev0987	1	8	39.86	7.97	≤ 19	1.0	$(1.8^{+0.3}_{-1.8}) \times 10^2$	≤ 1.8	0.01	1.55
rev0988	1	8	33.88	6.78	≤ 19	1.0	$(1.7^{+0.3}_{-0.8}) \times 10^2$	≤ 2.0	0.01	1.08
rev0989	1	8	30.55	6.11	≤ 19	1.0	$(1.6^{+0.3}_{-1.6}) \times 10^2$	≤ 2.0	0.01	0.78
rev0992	1	8	28.06	5.61	≤ 19	1.0	$(1.3^{+0.3}_{-1.3}) \times 10^2$	≤ 2	0.01	0.35
rev0993	1	8	60.44	12.09	$0.01^{+0.09}_{-0.00}$	1.0	$(1.6^{+0.2}_{-1.5}) \times 10^2$	≤ 1.1	0.01	1.04
rev0994	1	8	16.89	3.38	≤ 19	1.0	$(1.1^{+0.1}_{-1.1}) \times 10^2$	≤ 2	0.01	0.48
rev0995	1	8	31.34	6.27	≤ 19	1.0	$(1.8^{+0.1}_{-1.7}) \times 10^2$	≤ 2	0.01	0.73
rev0996	1	8	33.86	6.77	≤ 19	1.0	$(1.4^{+0.0}_{-1.3}) \times 10^2$	≤ 1.8	0.01	0.69
rev0998	1	8	61.20	12.24	≤ 19	1.0	$(1.3^{+0.0}_{-1.2}) \times 10^2$	≤ 1.3	0.01	0.51
rev0983	2	8	32.02	6.40	≤ 19	1.0	$(2^{+0}_{-2}) \times 10^2$	≤ 2	0.02	1.87
rev0985	2	8	32.02	6.40	≤ 19	1.0	$(3^{+1}_{-2}) \times 10^2$	≤ 2	0.02	1.75
rev0986	2	8	22.89	4.58	≤ 19	1.0	$(2^{+0}_{-2}) \times 10^2$	≤ 2	0.02	2.37
rev0987	2	8	21.81	4.36	≤ 19	1.0	$(2^{+0}_{-2}) \times 10^2$	≤ 2	0.02	2.57
rev0988	2	8	22.60	4.52	≤ 19	1.0	$(2^{+0}_{-2}) \times 10^2$	≤ 2	0.02	1.69
rev0989	2	8	26.24	5.25	≤ 19	1.0	$(2^{+0}_{-2}) \times 10^2$	≤ 2	0.02	1.57
rev0992	2	8	8.23	1.65	≤ 19	1.0	$(1.6^{+0.3}_{-1.6}) \times 10^2$	≤ 3	0.01	0.55
rev0993	2	8	34.69	6.94	≤ 19	1.0	$(1.8^{+0.2}_{-1.7}) \times 10^2$	≤ 1.7	0.01	1.50
rev0994	2	8	15.26	3.05	≤ 19	1.0	$(1.6^{+0.3}_{-1.5}) \times 10^2$	≤ 3	0.01	1.11
rev0995	2	8	22.80	4.56	≤ 19	1.0	$(2^{+0}_{-2}) \times 10^2$	≤ 2	0.02	1.14
rev0996	2	8	30.71	6.14	≤ 19	1.0	$(1.7^{+0.2}_{-1.6}) \times 10^2$	≤ 2.0	0.01	1.10
rev0998	2	8	36.56	7.31	≤ 19	1.0	$(1.5^{+0.2}_{-1.4}) \times 10^2$	≤ 1.8	0.01	0.75

Table A.16: Best fit parameters of the broken power law model with a Fe K α line of the combined spectra

Revolution	DOF	χ^2	χ^2_{red}	Norm [keV $^{-1}$ s $^{-1}$ cm $^{-2}$]	Γ_1	Γ_2	AreaGauss [photons s $^{-1}$ cm $^{-2}$]	C ₁	C ₂	C ₃
rev0983	65	119.26	2.02	9 $^{+15}_{-7}$	2.4 $^{+0.4}_{-0.6}$	2.646 \pm 0.020	0.08 $^{+0.07}_{-0.06}$	1.00	0.54	0.61
rev0985	65	92.50	1.57	8 $^{+19}_{-6}$	2.4 $^{+0.4}_{-0.6}$	2.427 \pm 0.019	0.05 $^{+0.06}_{-0.05}$	1.00	0.53	0.58
rev0986	65	78.84	1.34	9 $^{+19}_{-7}$	2.5 $^{+0.4}_{-0.5}$	2.46 $^{+0.03}_{-0.02}$	0.05 \pm 0.05	1.00	0.89	1.05
rev0987	65	95.09	1.61	9 $^{+15}_{-6}$	2.3 $^{+0.4}_{-0.6}$	2.56 \pm 0.02	0.09 \pm 0.07	1.00	0.62	0.73
rev0988	62	70.03	1.25	9 $^{+19}_{-6}$	2.6 $^{+0.4}_{-0.5}$	2.49 \pm 0.04	0.03 $^{+0.04}_{-0.03}$	1.00	0.97	1.10
rev0989	66	92.23	1.54	9 $^{+14}_{-6}$	2.4 $^{+0.4}_{-0.6}$	2.52 \pm 0.02	0.06 \pm 0.05	1.00	0.52	0.63
rev0992	57	68.49	1.34	16 $^{+21}_{-11}$	2.8 $^{+0.4}_{-0.5}$	2.80 \pm 0.03	0.03 $^{+0.05}_{-0.03}$	1.00	0.36	0.41
rev0993	67	105.50	1.73	11 $^{+16}_{-8}$	2.5 $^{+0.4}_{-0.5}$	2.86 \pm 0.02	0.07 $^{+0.06}_{-0.05}$	1.00	0.62	0.74
rev0994	55	80.94	1.65	17 $^{+25}_{-12}$	2.8 $^{+0.4}_{-0.5}$	2.86 \pm 0.03	0.04 $^{+0.05}_{-0.04}$	1.00	0.70	0.87
rev0995	60	85.27	1.58	6 $^{+4}_{-4}$	2.5 $^{+0.4}_{-0.6}$	2.76 \pm 0.03	0.02 $^{+0.04}_{-0.02}$	1.00	0.66	0.73
rev0996	63	73.60	1.29	14 $^{+20}_{-10}$	2.6 $^{+0.4}_{-0.5}$	2.92 \pm 0.03	0.06 $^{+0.06}_{-0.05}$	1.00	0.58	0.71
rev0998	57	75.23	1.48	14 $^{+17}_{-9}$	2.8 $^{+0.3}_{-0.4}$	2.81 \pm 0.04	0.04 $^{+0.04}_{-0.03}$	1.00	0.68	0.82

Table A.17: Best fit parameters of the broken power law model with a Fe K α line and an exponential cutoff of the combined spectra

Revolution	DOF	χ^2	χ^2_{red}	Norm [keV $^{-1}$ s $^{-1}$ cm $^{-2}$]	Γ_1	Γ_2	Area $_{\text{Gauss}}$ [photons s $^{-1}$ cm $^{-2}$]	E_{cut} [keV]	E_{fold} [keV]	c_1	c_2	c_3
rev0983	65	97.27	1.71	12 $^{+16}_{-3}$	2.5 $^{+0.4}_{-0.5}$	2.46 $^{+0.09}_{-0.07}$	0.06 $^{+0.06}_{-0.05}$	20 $^{+14}_{-0}$	(3 $^{+2}_{-1}$) \times 10 2	1.00	0.62	0.69
rev0985	65	76.41	1.34	8 $^{+19}_{-6}$	2.4 $^{+0.4}_{-0.6}$	2.40 \pm 0.02	0.05 \pm 0.05	(1.00 $^{+0.00}_{-0.07}$) \times 10 2	(3 $^{+2}_{-1}$) \times 10 2	1.00	0.54	0.60
rev0986	65	72.23	1.27	10 $^{+14}_{-7}$	2.6 $^{+0.4}_{-0.5}$	2.33 $^{+0.10}_{-0.09}$	0.04 $^{+0.05}_{-0.04}$	20 $^{+27}_{-0}$	(0.4 $^{+0.7}_{-0.2}$) \times 10 3	1.00	0.97	1.14
rev0987	65	66.24	1.16	12 $^{+17}_{-8}$	2.5 $^{+0.4}_{-0.5}$	2.29 \pm 0.09	0.06 $^{+0.06}_{-0.05}$	20 $^{+7}_{-0}$	(1.8 $^{+0.8}_{-0.4}$) \times 10 2	1.00	0.74	0.87
rev0988	62	62.14	1.15	9 $^{+12}_{-6}$	2.7 $^{+0.4}_{-0.5}$	2.32 $^{+0.12}_{-0.15}$	0.03 \pm 0.03	27 $^{+10}_{-7}$	(0.2 $^{+0.4}_{-0.1}$) \times 10 3	1.00	1.10	1.25
rev0989	66	80.54	1.39	9 $^{+14}_{-6}$	2.5 $^{+0.4}_{-0.6}$	2.50 \pm 0.02	0.06 \pm 0.05	(1.00 $^{+0.00}_{-0.06}$) \times 10 2	(0.2 $^{+0.3}_{-0.1}$) \times 10 3	1.00	0.53	0.64
rev0992	57	59.56	1.22	16 $^{+20}_{-11}$	2.8 $^{+0.4}_{-0.5}$	2.61 $^{+0.15}_{-0.11}$	0.03 $^{+0.04}_{-0.03}$	20 $^{+19}_{-0}$	(0.2 $^{+0.5}_{-0.1}$) \times 10 3	1.00	0.41	0.46
rev0993	67	60.52	1.03	19 $^{+20}_{-11}$	2.8 $^{+0.3}_{-0.4}$	2.54 \pm 0.08	0.04 \pm 0.04	20 $^{+4}_{-0}$	(1.4 $^{+0.5}_{-0.3}$) \times 10 2	1.00	0.75	0.90
rev0994	55	70.67	1.50	17 $^{+17}_{-8}$	2.9 $^{+0.3}_{-0.5}$	2.73 $^{+0.07}_{-0.16}$	0.04 \pm 0.04	31 $^{+8}_{-11}$	(0.3 $^{+0.3}_{-0.1}$) \times 10 3	1.00	0.78	0.97
rev0995	60	65.22	1.25	7 $^{+8}_{-5}$	2.7 $^{+0.3}_{-0.5}$	2.44 $^{+0.12}_{-0.13}$	0.02 $^{+0.03}_{-0.02}$	20 $^{+7}_{-0}$	(1.3 $^{+0.8}_{-0.4}$) \times 10 2	1.00	0.81	0.90
rev0996	63	53.04	0.96	18 $^{+21}_{-11}$	2.9 $^{+0.3}_{-0.4}$	2.64 \pm 0.11	0.04 \pm 0.04	20 $^{+8}_{-0}$	(1.5 $^{+0.9}_{-0.4}$) \times 10 2	1.00	0.69	0.84
rev0998	57	52.50	1.07	19 $^{+19}_{-11}$	3.1 $^{+0.3}_{-0.4}$	2.49 \pm 0.12	0.03 \pm 0.03	20 $^{+8}_{-0}$	(1.2 $^{+0.7}_{-0.3}$) \times 10 2	1.00	0.82	0.99

Table A.18: Best fit parameters of the compTT model with a Fe K α line of the combined spectra

Revolution	DOF	χ^2	χ^2_{red}	Norm	T_0 [keV]	kT [keV]	τ_p	Compton-y	Area _{Gauss} [photons s ⁻¹ cm ⁻²]	c ₁	c ₂	c ₃
rev0983	65	107.06	1.81	≤ 19	1.0	$(2.2^{+0.2}_{-0.8}) \times 10^2$	$0.01^{+0.03}_{-0.00}$	0.02	0.08 ± 0.02	1.00	0.59	0.66
rev0985	65	89.17	1.51	≤ 19	1.0	$(3.1^{+0.1}_{-0.9}) \times 10^2$	$0.010^{+0.017}_{-0.000}$	0.02	$0.064^{+0.017}_{-0.016}$	1.00	0.57	0.63
rev0986	65	77.82	1.32	≤ 19	1.0	$(3.0^{+0.1}_{-1.2}) \times 10^2$	$0.01^{+0.03}_{-0.00}$	0.02	$0.069^{+0.017}_{-0.016}$	1.00	0.96	1.12
rev0987	65	73.55	1.25	$0.014^{+0.007}_{-0.005}$	1.0	$(1.2^{+0.9}_{-0.4}) \times 10^2$	$0.09^{+0.13}_{-0.07}$	0.08	0.09 ± 0.02	1.00	0.71	0.83
rev0988	62	70.16	1.25	≤ 19	1.0	$(2.1^{+0.8}_{-1.2}) \times 10^2$	$0.02^{+0.15}_{-0.01}$	0.04	0.055 ± 0.013	1.00	1.05	1.19
rev0989	66	89.96	1.50	≤ 19	1.0	$(2.8^{+0.1}_{-0.8}) \times 10^2$	$0.010^{+0.015}_{-0.000}$	0.02	$0.074^{+0.018}_{-0.017}$	1.00	0.56	0.68
rev0992	57	64.91	1.27	≤ 19	1.0	$(2.0^{+0.1}_{-1.0}) \times 10^2$	$0.01^{+0.07}_{-0.00}$	0.02	0.06 ± 0.02	1.00	0.39	0.44
rev0993	67	77.25	1.27	$0.016^{+0.006}_{-0.005}$	1.0	$(0.9^{+0.5}_{-0.3}) \times 10^2$	$0.08^{+0.10}_{-0.06}$	0.06	0.077 ± 0.017	1.00	0.71	0.85
rev0994	55	77.63	1.58	≤ 19	1.0	$(1.6^{+0.3}_{-0.8}) \times 10^2$	$0.02^{+0.08}_{-0.01}$	0.02	$0.068^{+0.020}_{-0.019}$	1.00	0.77	0.95
rev0995	60	76.34	1.41	$0.009^{+0.006}_{-0.005}$	1.0	$(0.9^{+1.1}_{-0.4}) \times 10^2$	$0.10^{+0.20}_{-0.09}$	0.07	0.031 ± 0.011	1.00	0.75	0.83
rev0996	63	65.32	1.15	$0.013^{+0.008}_{-0.005}$	1.0	$(1.1^{+0.8}_{-0.4}) \times 10^2$	$0.05^{+0.12}_{-0.04}$	0.04	0.070 ± 0.017	1.00	0.66	0.79
rev0998	57	66.17	1.30	$0.011^{+0.007}_{-0.005}$	1.0	$(0.9^{+0.9}_{-0.4}) \times 10^2$	$0.1^{+0.2}_{-0.1}$	0.07	$0.071^{+0.012}_{-0.011}$	1.00	0.77	0.93

Bibliography

- Belloni T.M., 2010, In: T. Belloni (ed.) Lecture Notes in Physics, Berlin Springer Verlag, Vol. 794. Lecture Notes in Physics, Berlin Springer Verlag, p.53
- Bowyer S., Byram E.T., Chubb T.A., Friedman H., 1965, Science 147, 394
- Brocksopp C., Fender R.P., Larionov V., et al., 1999, MNRAS 309, 1063
- Cadolle Bel M., Goldwurm A., Rodriguez J., et al., 2006, In: Barret D., Casoli F., Lagache G., Lecavelier A., Pagani L. (eds.) SF2A-2006: Semaine de l’Astrophysique Francaise., p.119
- Chernyakova M., Kretschmar P., Neronov A., et al., 2010, JEM-X Analysis User Manual 9.3
http://isdcu3.unige.ch/Soft/download/osa/osa_doc/osa_doc-9.0/osa_um_jemx-9.3.pdf
- Chernyakova M., Neronov A., 2010, IBIS Analysis User Manual 9.2
http://isdcu3.unige.ch/Soft/download/osa/osa_doc/osa_doc-9.0/osa_um_ibis-9.2.pdf
- Davis J.E., 2001, ApJ 548, 1010
- Fender R., 2010, In: T. Belloni (ed.) Lecture Notes in Physics, Berlin Springer Verlag, Vol. 794. Lecture Notes in Physics, Berlin Springer Verlag, p.115
- Fender R.P., Homan J., Belloni T.M., 2009, MNRAS 396, 1370
- Friend D.B., Castor J.I., 1982, ApJ 261, 293
- Fritz S., 2008, Ph.D. thesis, Universität Tübingen
- Fürst F., 2010, Diploma thesis, Universität Erlangen-Nürnberg, Dr.-Remeis Sternwarte
- Gallo E., 2010, In: T. Belloni (ed.) Lecture Notes in Physics, Berlin Springer Verlag, Vol. 794. Lecture Notes in Physics, Berlin Springer Verlag, p.85
- Gallo E., Fender R.P., Pooley G.G., 2003, MNRAS 344, 60
- Gies D.R., Bolton C.T., Fender R., et al., 2003, In: American Astronomical Society Meeting Abstracts, Vol. 35. Bulletin of the American Astronomical Society, p.1332
- Grinberg V., 2010, Diploma thesis, Ludwig-Maximilians-Universität München, Dr.-Remeis Sternwarte
- Grinberg V., Cadolle Bel M., Pottschmidt K., et al., 2011a, In: J.-U. Ness & M. Ehle (ed.) The X-ray Universe 2011, Presentations of the Conference held in Berlin, Germany, 27-30 June 2011. Available online at: http://xmm.esac.esa.int/external/xmm_science/workshops/2011symposium/, p.261., p.261

-
- Grinberg V., Popp A., Marcu D., 2011b, Cygnus X-1: shedding light on the spectral variability of black holes, poster at "Black Hole Astrophysics: Tales of Power and Destruction", Winchester, UK, 18-22 July 2011
- Grove J.E., Johnson W.N., Kroeger R.A., et al., 1998, *ApJ* 500, 899
- Hanke M., 2007, Diploma thesis, Universität Erlangen-Nürnberg, Dr.-Remeis Sternwarte
- Herrero A., Kudritzki R.P., Gabler R., et al., 1995, *A&A* 297, 556
- Houck J.C., 2002, In: G. Branduardi-Raymont (ed.) High Resolution X-ray Spectroscopy with XMM-Newton and Chandra.
- Houck J.C., Denicola L.A., 2000, In: N. Manset, C. Veillet, & D. Crabtree (ed.) *Astronomical Data Analysis Software and Systems IX*, Vol. 216. Astronomical Society of the Pacific Conference Series, p.591
- <http://heasarc.gsfc.nasa.gov/docs/uhuru/uhuru.html> N., , The Uhuru Satellite, Webpage 2003
- <http://www.sciops.esa.int/index.php?project=INTEGRAL> E., , About INTEGRAL, Webpage 2010
- Hutchings J.B., 1978, *ApJ* 226, 264
- in't Zand J.J.M., 1992, Ph.D. thesis, Space Research Organization Netherlands, Sorbonnelaan 2, 3584 CA Utrecht, The Netherlands
- Karttunen H., Kröger P., Oja H., et al., 2007, *Fundamental Astronomy*, Springer
- Markoff S., 2010, In: T. Belloni (ed.) *Lecture Notes in Physics*, Berlin Springer Verlag, Vol. 794. *Lecture Notes in Physics*, Berlin Springer Verlag, p.143
- McConnell M.L., Ryan J.M., Collmar W., et al., 2000, *ApJ* 543, 928
- McConnell M.L., Zdziarski A.A., Bennett K., et al., 2002, *ApJ* 572, 984
- Oppenheimer J.R., Volkoff G.M., 1939, *Physical Review* 55, 374
- Stirling A.M., Spencer R.E., de la Force C.J., et al., 2001, *MNRAS* 327, 1273
- Titarchuk L., 1994, *ApJ* 434, 570
- Uttley P., McHardy I.M., Papadakis I.E., 2002, *MNRAS* 332, 231
- Uttley P., McHardy I.M., Vaughan S., 2005, *MNRAS* 359, 345
- Webster B.L., Murdin P., 1972, *Nature* 235, 37
- Wilms J., Nowak M.A., Pottschmidt K., et al., 2006, *A&A* 447, 245
- Ziółkowski J., 2005, *Chinese Journal of Astronomy and Astrophysics Supplement* 5, 75

Erklärung

Hiermit bestätige ich, dass ich diese Arbeit selbstständig und nur unter Verwendung der angegebenen Hilfsmittel angefertigt habe.

Erlangen, den 19.09.2011

Alexander Popp